Charge exchange and excitation in $H+He^{2+}$ and $He^{+}+H^{+}$ collisions using single- and multichannel perturbed-stationary-state propagators

Gabriel Hose
The James Franck Institute, The University of Chicago, Chicago, Illinois 60637
(Received 20 June 1994)

Our recently formulated (preceding paper, PP I) semiclassical perturbed-stationary-state single- and multichannel propagators are applied to study the collisions of He^{2+} on $H(1s)$ and H^{+} on $He^{+}(1s)$, including as many as 45 molecular adiabatic states unmodified by an electron translation factor. In the energy range below the collisional ionization threshold, a multichannel eikonal propagator with 45 states reproduces the total charge-exchange cross sections—a feat that a single-channel theory cannot accomplish, as convergence with respect to the basis size indicates conclusively. In this region of negligible ionization, the 45-state multichannel cross sections are also in reasonably good agreement with other semiclassical calculations that employ either atomic or molecular basis functions modified by translation factors. Regarding level-selective cross sections, however, our results and previous translation-factor-based predictions are far apart. The multichannel propagator yields higher cross sections for transfer into excited states whose participation is artificially attenuated in the other models by the translation factor. In light of our findings, we discuss recent experimental measurements of uv emission induced in collisions of hydrogen and α particles and suggest an interpretation that invokes optical interference to explain the observed Balmer-α cross sections and, perhaps, also the slightly low radiative-quenching yield of the product metastable helium ion.

PACS number(s): 34.10.+x, 34.50.Pi, 34.70.+e

I. INTRODUCTION

During the past two decades, many studies [1–25] have been conducted to simulate electron-capture reactions measured in $H(1s)+He^{2+}$ [26–33] and $He^{+}(1s)+H^{+}$ [34–40] collisions. These are the simplest examples of nonresonant charge transfer prevalent in larger more complicated systems. But the breadth of theoretical work [1–25] is brought about also because, being small one-electron systems for which the exact electron wave functions are analytically known, they are proving grounds for theoretical models of charge-exchange collisions.

Figure 1 depicts the total cross sections for charge exchange [27,28,30,35–39] as well as ionization [40–43], against the relative target-projectile velocity, measured in collisions of α particles or protons impinging respectively, on ground-state hydrogen atom or helium ion targets. As seen, electron transfer reactions peak when the collision velocity is comparable to the velocity of the electron in the target state, i.e., 1 a.u. in hydrogen atoms and about 1.4 a.u. in helium ions. Indeed, throughout the velocity range for charge exchange (and most of the ionization regime), the expectation value of the target electron velocity is still sufficiently high to suggest noticeable mixing and distortion of target and capture states. Charge-exchange collisions are thus treated [1–25,44–54] within a semiclassical close-coupling scheme that accounts for the complex interactions between the quantum electron states to infinite order, while the much heavier nuclei are assumed to be moving practically undisturbed along a straight-line classical trajectory.

The various theoretical models of atomic collisions may be classified by two prototypes. One employs a close-coupling basis comprising products of asymptotic atomic functions centered on the two colliding nuclei [4,5,44–47]. The second group of perturbed-stationary-

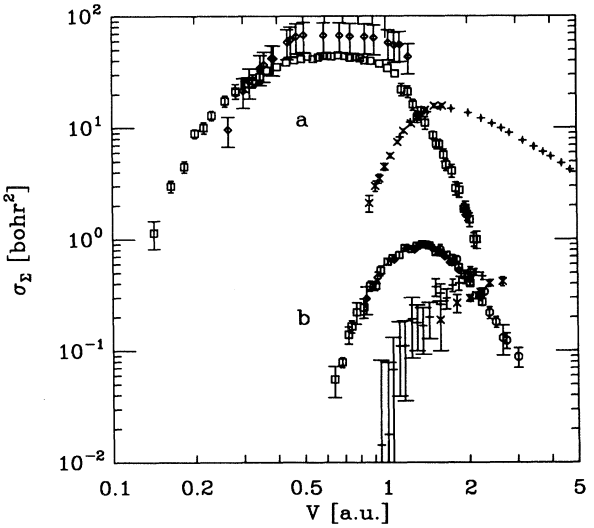

FIG. 1. Total cross section for electron capture (□,○,◇) and ionization (×,+) as a function of the relative target-projectile velocity measured in collisions of (curves *a*) $H(1s)+He^{2+}$ and (curves *b*) $He^{+}(1s)+H^{+}$. The electron-capture data are taken from (a) (□) Shah and Gilbody [27], Nutt *et al.* [30]; (◇) Bayfield and Khayrallah [28]; (b) (○) Angel *et al.* [37]; Watts, Dunn, and Gilbody [40]; (◇) Peart, Rinn, and Dolder [38]; (□) Rinn, Melchert, and Salzborn [39]. The ionization results are from (a) (×) Shah and Gilbody [41]; (+) Shah *et al.* [43]; (b) (×) Watts, Dunn, and Gilbody [40], and (+) Rinn *et al.* [42]. Error bars reflect the reported standard deviation of each point.

state (PSS) methods [1–3,48–52,54] expands the electronic wave function on a basis of molecular adiabatic states. In both approaches the basis functions are usually modified [3–25,44,48] by a nuclear-velocity phaselike term known as the electron translation factor (ETF). This modification is considered necessary [44–52] in order to alleviate the momentum transfer problem, namely, the existence of finite asymptotic dynamical couplings between capture states of the electron. There is also an added advantage when using atomic bases that contain nonorthogonal functions centered on different nuclei, since at low impact parameters it is virtually impossible to perform a numerically accurate close-coupling calculation without translation factors. At close range, the troublesome two-center overlap integrals are largely reduced due to the ETF modification of the atomic basis functions. The adiabatic basis, on the other hand, is strictly orthonormal [1,2,54] offering no numerical complications over the entire impact-parameter range. Here the sole *raison d'être* for the ETF is to eliminate asymptotic dynamical couplings and at the same time ensure Galilean invariance [48–52]. The translation-factor approach is not without criticism though [47,49,51,53]. A major difficulty is that the ETF is conceived on asymptotic reasoning insufficient to solidify its precise form, especially in the reactive molecular region. Hence a translation factor is not unique. Several rather different prescriptions for optimized ETF are currently being used, and all [3–25], more or less, reproduce the total charge-exchange cross sections of Fig. 1 below the ionization threshold.

The present study purposely aims at showing that a multichannel PSS approximation [54] without a translation factor provides a reliable description of electron transfer reactions in collisions of $H(1s)+He^{2+}$ and $He^{+}(1s)+H^{+}$. The cross sections calculated using the multichannel PSS propagator converge to the experimental data below ionization as the size of the finite (bound-electron) adiabatic basis is increased. In this range, the accuracy of our total charge-exchange cross sections obtained with 30–45 molecular orbitals is at least as good as those calculated from ETF-modified bases [3–25]. However, there is disagreement between the present and previous calculations regarding the transfer into select levels. In fact, for the capture from hydrogen atom the multichannel PSS simulations reveal a mechanism significantly different from translation-factor theories, emphasizing more the role played by the excited helium ion states. Section II provides a brief account of the translationally invariant single- and multichannel PSS theories formulated in [54]. The computation of adiabatic molecular orbitals and the dynamical couplings in spheroidal coordinates is summarized in Sec. III. Eikonal calculations using single- and multichannel propagators are presented in Secs. IV and V, respectively. In Sec. V we also analyze the relationship between the capture reaction and the following Lyman and Balmer emissions, and suggest that optical interference effects might have been observed in recent charge-transfer experiments [31–33]. Although functions representing ionization are omitted from our PSS basis, cross sections are simulated above the collisional ionization threshold and throughout the entire charge-exchange range. Atomic units ($\hbar=1$, $m_e=1$, $e=1$) are used everywhere below.

II. THEORY

We are interested in a molecule made of an α particle, a proton, and one electron, whose instantaneous positions in the laboratory frame are given by the vectors $\mathbf{X}_{He}$, $\mathbf{X}_H$, and $\mathbf{X}_e$, respectively. Neglecting electron mass polarization, the electronic Born-Oppenheimer (BO) Hamiltonian for this system is

$$H_{BO}(\mathbf{R},\mathbf{r})=-\tfrac{1}{2}\Delta_r-\frac{2}{|\mathbf{r}+q\mathbf{R}|}-\frac{1}{|\mathbf{r}-p\mathbf{R}|}\ , \tag{1}$$

where $\mathbf{R}$ and $\mathbf{r}$ are the internal vectors defined [52,54,56] below:

$$\mathbf{R}=\mathbf{X}_H-\mathbf{X}_{He},\quad \mathbf{r}=\mathbf{X}_e-p\mathbf{X}_{He}-q\mathbf{X}_H,\quad p+q=1\ . \tag{2}$$

As usual, the electron is described in a body-fixed frame such that its $\hat{\mathbf{z}}$ axis coincides with the internuclear vector $\mathbf{R}$ [51,55,56]. The sets of adiabatic orbitals and electron energies satisfying

$$H_{BO}(\mathbf{R},\mathbf{r})\psi_\alpha(\mathbf{R},\mathbf{r})=U_\alpha(R)\psi_\alpha(\mathbf{R},\mathbf{r})\ , \tag{3}$$

with H_{BO} given by (1), separate into three pairable subsets: $\{\psi_\alpha^{He}\},\{U_\alpha^{He}\}$; $\{\psi_\alpha^{H}\},\{U_\alpha^{H}\}$; and $\{\psi_\alpha^{I}\},\{U_\alpha^{I}\}$. The subsets $\{\psi_\alpha^{He}\}$ or $\{\psi_\alpha^{H}\}$ contain the bound-electron molecular orbitals that in the limit $R\to 0$ go to Li^{2+} states [57]. The label α for these orbitals may thus be taken as the united-atom principal, angular, and magnetic quantum numbers. The orbitals $\{\psi_\alpha^{I}\}$ are adiabatic continuum states describing ionization of the molecular electron. Like the bound molecular orbitals, the adiabatic ionization functions depend on R parametrically, but their corresponding electron energies, in contradistinction, are constant. This is because the ionization spectrum $\{U_\alpha^{I}\}$ is continuous.

On dissociation, the bound molecular orbitals $\{\psi_\alpha^{He}\}$ and $\{\psi_\alpha^{H}\}$ become zero-field Stark states [57] localized on the helium and hydrogen nuclei, respectively. That is, they turn into linear combinations of degenerate atomic orbitals either from $\{\phi_{n,lm}^{He^+}\}$ or $\{\phi_{n,lm}^{H}\}$ at the limiting atomic energies $\{U_n^{He^+}\}$ or $\{U_n^{H}\}$, i.e.,

$$\lim_{R\to\infty}\psi_\alpha^{He}(\mathbf{R},\mathbf{r})\to\sum_{l=|m|}^{n-1}\langle n,l,m|\alpha\rangle\phi_{nlm}^{He^+}(\mathbf{r}+q\mathbf{R})\ ,$$
$$\lim_{R\to\infty}U_\alpha^{He}(R)\to U_n^{He^+}\ , \tag{4a}$$

$$\lim_{R\to\infty}\psi_\alpha^{H}(\mathbf{R},\mathbf{r})\to\sum_{l=|m|}^{n-1}\langle n,l,m|\alpha\rangle\phi_{nlm}^{H}(\mathbf{r}-p\mathbf{R})\ ,$$
$$\lim_{R\to\infty}U_\alpha^{H}(R)\to U_n^{H}\ , \tag{4b}$$

where n and l are the asymptotic principal and centrifugal quantum numbers, and m is identical with the united-atom magnetic number corresponding to ψ_α. The Stark coefficients $\{\langle n,l,m|\alpha\rangle\}$ are independent of the asymptotic localization nucleus, and for any n,m pair may be obtained by diagonalizing a tridiagonal matrix $T^{n,m}$ with a zero diagonal and a subdiagonal given by

$$T^{n,m}_{l+1,l}=\left[\frac{[(l+1)^2-m^2][n^2-(l+1)^2]}{(2l+1)(2l+3)}\right]^{1/2},$$
$$l=|m|,\ldots,n-1\ . \quad (5)$$

The $n-|m|$ eigenvalues of $T^{n,m}$ appear in the inverse order of the united-atom centrifugal numbers labeling the $n-|m|$ asymptotically degenerate adiabatic orbitals [57].

In the semiclassical perturbed-stationary-state approximation [1,2,48–54] the wave function of the electron is assumed to evolve on the collision time scale according to the Schrödinger equation

$$i\frac{d\Psi}{dt}=H_{\rm BO}\Psi\ , \quad (6)$$

where $H_{\rm BO}$ is the (time-dependent) electronic Hamiltonian (1). The adiabatic orbital basis $\{\psi_\alpha\}$ associated with (1), being the direct sum $\{\psi^{\rm He}_\alpha\}\oplus\{\psi^{\rm H}_\alpha\}\oplus\{\psi^{I}_\alpha\}$, is actually suitable to expand an electronic wave function Ψ covering all three rearrangement channels observed in Fig. 1. Here, however, the PSS expansion is limited to span only the charge-exchange rearrangements $H+He^{2+}$ and $He^{+}+H^{+}$, i.e.,

$$\Psi(t)=\sum_{n={\rm He,H}}\sum_{\alpha\in n}a^n_\alpha(t)\psi^n_\alpha\ . \quad (7)$$

Even if this expansion covers the entire bound-state manifold, we only expect it to accurately reproduce the features seen in Fig. 1 up to collision velocities of about 0.7 a.u., since above this value the ionization channel $He^{2+}+H^{+}+e^{-}$ is evidently important in Fig. 1.

Assuming straight-line nuclear trajectories and substituting (7) for the electronic wave function, the Schrödinger equation (6) is transformed [54] into a set of spatial coupled differential equations for the amplitudes $\{a^m_\alpha\}$,

$$i\frac{da^m_\alpha}{dZ}=\sum_{n={\rm He,H}}\sum_{\beta\in n}\langle\psi^m_\alpha|G(Z,b,E)|\psi^n_\beta\rangle a^n_\beta\ . \quad (8)$$

In the coupled equations above G is a propagator that depends on the nuclear Z coordinate, the impact parameter b, and the scattering energy E. We distinguish [54] between single- and multichannel propagators. A single-channel propagator originates from the scattering momentum operator associated with one charge-exchange channel. Thus two single-channel propagators, $G_{\rm He}$ and $G_{\rm H}$, exist in our system, respectively corresponding to the asymptotic rearrangements $He^{+}+H^{+}$ and $H+He^{2+}$. The matrix elements of the eikonal propagator G_l (l=He or H) are given by

$$\langle\psi^m_\alpha|G_l(Z,b,E)|\psi^n_\beta\rangle=V_l^{-1}U_\alpha\delta_{\alpha,\beta}-iR^{-1}\langle\psi^m_\alpha|ZA^R_l-bA^\theta_l|\psi^n_\beta\rangle\ , \quad (9)$$

where $R=(Z^2+b^2)^{1/2}$ is the internuclear distance; $V_l=(2\mu_l^{-1}E)^{-1/2}$ is the channel velocity determined from the appropriate reduced mass, either $\mu_{\rm He}=[(m_{\rm He}+1)^{-1}+m_{\rm H}^{-1}]^{-1}$ or $\mu_{\rm H}=[m_{\rm He}^{-1}+(m_{\rm H}+1)^{-1}]^{-1}$; and A^R_l and A^θ_l are the radial and angular components of the invariant electronic coupling [54,56]

$$A^R_{\rm He}=\frac{\partial}{\partial R}-q\frac{\partial}{\partial z},\quad A^\theta_{\rm He}=-iR^{-1}L_y-q\frac{\partial}{\partial x}\ , \quad (10a)$$

$$A^R_{\rm H}=\frac{\partial}{\partial R}+p\frac{\partial}{\partial z},\quad A^\theta_{\rm H}=-iR^{-1}L_y+p\frac{\partial}{\partial x}\ . \quad (10b)$$

The propagator matrix elements (9) are easily computed once the radial and angular couplings $\langle\psi^m_\alpha|A^R_l|\psi^n_\beta\rangle$ and $\langle\psi^m_\alpha|A^\theta_l|\psi^n_\beta\rangle$ are known as a function of the internuclear separation (see Sec. III). The multichannel propagator defined by

$$G(Z,b,E)=G_{\rm He}(Z,b,E)\sum_{\alpha\in{\rm He}}|a^{\rm He}_\alpha(Z,b,E)|^2+G_{\rm H}(Z,b,E)\sum_{\alpha\in{\rm H}}|a^{\rm H}_\alpha(Z,b,E)|^2 \quad (11)$$

is the instantaneous adiabatic average of the two single-channel propagators $G_{\rm He}$ and $G_{\rm H}$. Accordingly, its matrix elements are obtained from (9) and (11) using the temporally propagated amplitudes $\{a^m_\alpha\}$.

Given the impact parameter b and the collision energy E, the coupling equations (8) are to be integrated in the nuclear $\hat{\mathbf{Z}}$ direction starting from a negative distant-past point Z_0^- up to a positive far-future coordinate Z_0^+. Choosing Z_0^- generally depends on the propagator and the initial state as discussed later. To determine the integration termination point the desired cross sections must be considered. When aiming for the total electron-transfer cross section Z_0^+ is picked such that all charge-exchange couplings are sufficiently small (approximately 50 bohr in the HeH^{2+} system investigated with our largest PSS basis). However, if state-to-state cross sections are required, then Z_0^+ should be significantly higher to ensure constant dynamical couplings and electronic energies [54]. Since in the invariant PSS formulation [54] finite residual asymptotic couplings exist, some of the propagated amplitudes $\{a^m_\alpha\}$ may oscillate indefinitely, and we need to extract from them the physical (inertial) amplitudes if final-state probabilities are sought for.

Let G^∞ be the asymptotic limit propagator matrix. In a single-channel theory the limit propagator matrix elements are independent of the impact parameter [54],

$$\begin{aligned}
&\langle\psi^{\rm He}_\alpha|G^\infty_{\rm He}(E)|\psi^{\rm He}_\beta\rangle=V_{\rm He}^{-1}U^{\rm He}_\alpha\delta_{\alpha,\beta}\ ,\\
&\langle\psi^{\rm He}_\alpha|G^\infty_{\rm He}(E)|\psi^{H}_\beta\rangle=\langle\psi^{\rm H}_\alpha|G^\infty_{\rm He}(E)|\psi^{\rm He}_\beta\rangle=0\ , \quad (12a)\\
&\langle\psi^{\rm H}_\alpha|G^\infty_{\rm He}(E)|\psi^{\rm H}_\beta\rangle=V_{\rm He}^{-1}U^{\rm H}_\alpha\delta_{\alpha,\beta}+i\langle\psi^{\rm H}_\alpha|\frac{\partial}{\partial z}|\psi^{\rm H}_\beta\rangle\ .
\end{aligned}$$

$$\begin{aligned}
&\langle\psi^{\rm He}_\alpha|G^\infty_{\rm H}(E)|\psi^{\rm He}_\beta\rangle=V_{\rm H}^{-1}U^{\rm He}_\alpha\delta_{\alpha,\beta}-i\langle\psi^{\rm He}_\alpha|\frac{\partial}{\partial z}|\psi^{\rm He}_\beta\rangle\ ,\\
&\langle\psi^{\rm He}_\alpha|G^\infty_{\rm H}(E)|\psi^{\rm H}_\beta\rangle=\langle\psi^{\rm H}_\alpha|G^\infty_{\rm H}(E)|\psi^{\rm He}_\beta\rangle=0\ , \quad (12b)\\
&\langle\psi^{\rm H}_\alpha|G^\infty_{\rm H}(E)|\psi^{\rm H}_\beta\rangle=V_{\rm H}^{-1}U^{\rm H}_\alpha\delta_{\alpha,\beta}\ .
\end{aligned}$$

The asymptotic matrix elements of the multichannel propagator (11) depend on the final rearrangement probabilities and are therefore a function of the impact parameter. Assuming electron transfer is complete at Z_0^+, the limit multichannel propagator elements are calculated using (12) and

$$G^{\infty}(b,E)=G^{\infty}_{\mathrm{He}}(E)\sum_{\alpha\in\mathrm{He}}|a^{\mathrm{He}}_{\alpha}(Z_0^+,b,E)|^2 + G^{\infty}_{\mathrm{H}}(E)\sum_{\alpha\in\mathrm{H}}|a^{\mathrm{H}}_{\alpha}(Z_0^+,b,E)|^2 . \quad (13)$$

The asymptotic limit propagators (12) and (13) are clearly block diagonal in the charge-exchange rearrangements. They may mix orbitals of the same atom because a captured electron travels in the entrance Jacobi coordinates [54]. The proper propagated asymptotic states satisfy, therefore, an eigenvalue equation for the traveling momenta $\{\eta_\gamma\}$,

$$G^{\infty}Y_\gamma=\eta_\gamma Y_\gamma , \quad (14)$$

and are linear combinations of asymptotic adiabatic basis orbitals localizing on the same nucleus [54,58], i.e.,

$$Y_{\gamma\in\mathrm{He}}=\sum_{\alpha\in\mathrm{He}}y_{\alpha,\gamma}\psi^{\mathrm{He}}_{\alpha}(R\to\infty) , \qquad Y_{\gamma\in\mathrm{H}}=\sum_{\alpha\in H}y_{\alpha,\gamma}\psi^{\mathrm{H}}_{\alpha}(R\to\infty) . \quad (15)$$

The traveling phase causing the propagated probabilities to oscillate indefinitely is then negated [54] by the following transformation that yields the final inertial amplitudes:

$$\chi^m_{\alpha}(Z_0^+,b,E)=\sum_{\gamma\in m}\sum_{\beta\in m}y^*_{\alpha,\gamma}\exp[+i\eta_\gamma Z_0^+]\times y^*_{\beta,\gamma}a^m_{\beta}(Z_0^+,b,E) . \quad (16)$$

The probability for an eikonal collision transition from the entrance ground state ϕ^k_{1s} ($k=\mathrm{He}^+$ or H) to the orbital $\phi^{k'}_{n'l'm'}$ ($k'=\mathrm{He}^+$ or H) at the impact parameter b and energy E is obtained from the amplitudes (16) after applying the inverse of the Stark transformation appropriate for the atomic quantum numbers n' and m',

$$W[\phi^{k'}_{n'l'm'}\leftarrow\phi^k_{1s};b,E]=\left|\sum_{\alpha\in k'}\langle\alpha|n'l'm'\rangle\chi^{k'}_{\alpha}(Z_0^+,b,E)\right|^2 . \quad (17)$$

The final transition probability W is constant if Z_0^+ is sufficiently large so that all couplings and electronic energies are numerically close to their limit. The corresponding state-to-state cross sections are then given by the usual semiclassical formula [50–52]

$$\sigma^{k'}_{n'l'm'}(E)=\sigma[\phi^{k'}_{n'l'm'}\leftarrow\phi^k_{1s};E]=2\pi\int W[\phi^{k'}_{n'l'm'}\leftarrow\phi^k_{1s};b,E]b\,db . \quad (18)$$

We now return to discuss the integration starting point and initial propagated amplitudes. Consider first the multichannel propagator or a single-channel propagator defined for the target rearrangement. In this case the propagator cannot couple the initial (undistorted) target states [54]. Also, the $1s$ ground states of hydrogen atom and helium ion are actually the asymptotic limits of the molecular orbitals $1s\sigma$ and $2p\sigma$, respectively. Hence here the initial amplitudes for $He^+(1s)+H^+$ are given from

$$a^m_{\alpha}(Z_0^-,b,E)=\exp[-iV^{-1}_{\mathrm{He}}U^{\mathrm{He}}_{1s}(Z_0^-)]\delta_{\mathrm{He},m}\delta_{1s\sigma,\alpha} , \quad (19a)$$

while for $H(1s)+He^{2+}$ we have

$$a^m_{\alpha}(Z_0^-,b,E)=\exp[-iV^{-1}_{\mathrm{H}}U^{\mathrm{H}}_{1s}(Z_0^-)]\delta_{\mathrm{H},m}\delta_{2p\sigma,\alpha} , \quad (19b)$$

with $Z_0^-=-(R_0^2+b^2)^{1/2}$ and R_0 the initial internuclear separation. The value of R_0 is chosen such that $Z_0^-=-35$ bohr for the $He^+(1s)+H^+$ collision, and 50 bohr in $H(1s)+He^{2+}$. The situation is slightly more complicated when the propagator is ill defined for the channel [54], i.e., G_{H} for a helium ion target or G_{He} for hydrogen. In this case we have to account for entrance asymptotic coupling reflecting the fact that the target electron travels in the "projectile" Jacobi frame. Thus Z_0^- is taken to be the same as Z_0^+ and the initial amplitudes are given [54] by formulas similar to (16), i.e.,

$$a^m_{\alpha}(Z_0^-,b,E)=\delta_{\mathrm{He},m}\sum_{\gamma\in\mathrm{He}}y_{\alpha,\gamma}\exp[-i\eta_\gamma Z_0^-]y_{1s\sigma,\gamma} \quad (20a)$$

for $He^+(1s)+H^+$ and

$$a^m_{\alpha}(Z_0^-,b,E)=\delta_{\mathrm{H},m}\sum_{\gamma\in H}y_{\alpha,\gamma}\exp[-i\eta_\gamma Z_0^-]y_{2p\sigma,\gamma} \quad (20b)$$

for $H(1s)+He^{2+}$.

III. MOLECULAR ORBITALS AND DYNAMICAL COUPLINGS

Expressing the body-fixed position of the electron in spheroidal coordinates, the Schrödinger equation (3) for the electronic BO Hamiltonian (1) of the HeH^{2+} molecule is factorized [59–61] into three one-dimensional differential equations and can be solved exactly. In forthcoming work [62] we report on the spheroidal-coordinate calculation of 66 electronic energy curves of HeH^{2+} and the associated molecular orbitals at 239 points in the range $0.01\le R\le 70$ bohr. Beginning from the united atom, the initial R mesh is 0.01 and it increases to 0.1, 0.2, 0.4, and 0.8 at the internuclear separations 0.1, 12, 18, and 32 bohr, respectively. The 20 electronic curves previously tabulated by Winter, Duncan, and Lane [61] are in agreement with ours to within the last figure. Also, from $R=50$ to 70 bohr, all reported 66 electronic energies [62] appear to be in excellent agreement with the energies computed using the perturbation formulas given by Power [57]. These 66 BO curves correspond asymptotically to the lowest three hydrogen and six helium ion energy levels. The current PSS study, however, does not include the 21 molecular curves dissociating to the (highest) $He^+(n=6)$ level. Furthermore, as the possible initial (ground) states $1s\sigma$ and $2p\sigma$ are both real and of even azimuthal (magnetic) parity, and since neither of the operators (10) can couple real magnetic even states to odd ones [62], collision simulations are conducted using some or all of the 45 real even states shown in Table I. The largest subspace $\{\psi^{\mathrm{He}}_{\alpha}\}$ comprises 35 states asymptotically span-

TABLE I. The 45 even adiabatic molecular orbitals of HeH^{2+} arranged in groups by the asymptotic atom, absolute magnetic number $|m|$, and energy number n.

Atom	$\|m\|$	n	HeH^{2+} orbitals[a]
He^+	0	1	$1s\sigma$
		2	$3d\sigma;2s\sigma$
		3	$4f\sigma;3p\sigma;3s\sigma$
		4	$6h\sigma;5f\sigma;4p\sigma;4s\sigma$
		5	$7i\sigma;6g\sigma;5d\sigma;5p\sigma;5s\sigma$
	1	2	$2p\pi$
		3	$3d\pi;3p\pi$
		4	$5g\pi;4d\pi;4p\pi$
		5	$6h\pi;5f\pi,5d\pi;5p\pi$
	2	3	$3d\delta$
		4	$4f\delta;4d\delta$
		5	$5g\delta;5f\delta;5d\delta$
	3	4	$4f\phi$
		5	$5g\phi;5f\phi$
	4	5	$5g\gamma$
H	0	1	$2p\sigma$
		2	$5g\sigma;4d\sigma$
		3	$8j\sigma;7h\sigma;6f\sigma$
	1	2	$4f\pi$
		3	$7i\pi;6g\pi$
	2	3	$6h\delta$

[a]United-atom notation. In the asymptotic limit each HeH^{2+} orbital is a linear combination of degenerate even atomic orbitals with $l=|m|,\ldots,n-1$.

ning the energy levels $n=1-5$ of He^+, while the maximum $\{\psi_\alpha^H\}$ covers the three lowest even levels of hydrogen atom. A measure of the numerical accuracy of these orbitals is provided by the difference between the overlap (by Gaussian quadrature) and the unit matrices. For $R>0.05$ bohr the maximum difference element was less than 10^{-6} [62]. The same actually holds for $R=0.05$ bohr and below with the exclusion of difference elements involving the $5s\sigma$ and lower $s\sigma$ orbitals, which are higher. Still the largest such difference involving the $4s\sigma$ state is only 10^{-3} at $R=0.01$ bohr.

The calculation in spheroidal coordinates of the radial and angular dynamical couplings between the molecular orbitals of Table I requires analytical as well as numerical one-dimensional differentiation and integration [62]. The accuracy of the coupling has been estimated by testing how well anti-Hermiticity holds. From $R=0.05$ bohr onward, and except for some couplings involving the orbitals $3s\sigma$, $4s\sigma$, and $5s\sigma$, the deviation from anti-Hermiticity is small [62]. For instance, the radial self-coupling, which is formally zero, is always absolutely less than 10^{-6} and usually is much smaller. As mentioned, the higher excited $s\sigma$ states may not be as numerically accurate below $R=0.05$ bohr. The worst radial self-coupling is 5×10^{-3} for the orbital $5s\sigma$ at $R=0.01$ bohr, but it immediately improves to under 5×10^{-4} at the next point. The couplings at very short R are collisionally not very important though, because they affect the results only at small impact parameters with negligible semiclassical weight [see (18)]. Generally, the numerical precision of any coupling element in the R range where it is collisionally significant is very good [62]. At large internuclear separations the relative accuracy tends to decrease [61] and many couplings are practically so small that they become erratic due to numerical errors. Such couplings were nullified at large R. All couplings at $R=70$ bohr were compared with their corresponding asymptotic value, and were found to be evolving correctly toward the limit. Nonzero residual radial $\langle\psi_\alpha^k|\partial/\partial z|\psi_\beta^k\rangle$ [see (12)] and angular $\langle\psi_\alpha^k|\partial/\partial x|\psi_\beta^k\rangle$ couplings have been obtained via a Stark transformation $\{\langle n,l,m|\alpha\rangle\}$ from the corresponding dipole-velocity elements between the hydrogenlike functions, $\langle n,l,m|\partial/\partial z|n'\neq n,l\pm1,m\rangle$ and $\langle n,l,m|\partial/\partial x|n'\neq n,l\pm1,m\pm1\rangle$ which are readily computed by numerical integration.

Our collision simulations cover a spatial range extending up to $R\approx400$ bohr. That is far beyond the outermost R at which the molecular orbitals (Table I), and the couplings among them, have been computed. For $R>70$ bohr the electronic energy curves are actually accurately known through the formulas provided by Power [57]. These formulas have been implemented in the scattering calculations beyond $R=70$ bohr. The dynamical couplings in this range have been extrapolated to the known (see above) asymptotic value using the last ten points from the molecular calculation (the couplings for $R>60$ bohr are usually very close to the $R\to\infty$ limit [62]). If the coupling is found to be monotonic over these ten points, it is exponentially fitted to the asymptote, and the result is used to compute the coupling at $R>70$ bohr. However, some of the couplings among the highly excited orbitals exhibit oscillatory behavior at large R with a period that slowly increases toward the asymptotic limit [62]. Because the amplitude of these oscillations is rather small, using the limit we linearly extrapolated oscillatory couplings from $R=70$ bohr onward.

IV. CHARGE-EXCHANGE CALCULATIONS USING SINGLE-CHANNEL PROPAGATORS

The eikonal coupled equations (8) are integrated along the $\hat{\mathbf{Z}}$ axis beginning from a negative distant-past point Z_0^- up to Z_0^+ in the positive far future. The single-channel propagator matrix (9) is computed along the trajectory Z from the electronic energies, the dynamical coupling matrix, the target-projectile velocity V_l, and the impact parameter b. Since the dynamical coupling elements are provided on a rather dense grid of the internuclear separation, they are linearly interpolated if $R=(Z^2+b^2)^{1/2}$ falls between grid points. The integration procedure is a standard fifth- and sixth-order Runge-Kutta algorithm. The numerical accuracy of the propagated probabilities is estimated from backward integration to be better than 10^{-12}. Target propagator calculations, namely, G_H for $H(1s)+He^{2+}$ and G_{He} for $He^+(1s)+H^+$, have been performed with the adiabatic bases described in Table II throughout the charge-exchange velocity range. The convergence with respect to the PSS basis of the computed total charge-exchange cross section as a function of the target-projectile velocity (the total electron transfer spectrum) is examined below.

Also reported for comparison are total charge-exchange results calculated at one velocity using the captured-electron (or projectile) propagators, i.e., G_{He} for $H(1s)+He^{2+}$ and G_H for $He^+(1s)+H^+$. We first discuss the total electron capture cross sections from the target propagator calculations.

A. G_H calculations for $H(1s)+He^{2+}\rightarrow H^+ + He^+$

Five total collisional electron transfer spectra computed with small to medium size adiabatic bases are displayed in Fig. 2 against the experimental results [27,30] including ionization [41,43]. Figure 3 compares the measured [27,30] charge-exchange cross section with the target propagator calculations for the largest four bases from Table II. A compilation of total cross sections at five selected velocities is given in Table III. The transfer cross section at the collision energy E is computed from the state capture cross sections via

$$\sigma_{\Sigma}^{He^+}(E)=\sigma[He^+\leftarrow H(1s);E]$$
$$=\sum_{n,m\in He^+}\sum_{l=|m|}^{n-1}\sigma[\phi_{n,l,m}^{He^+}\leftarrow\phi_{1s}^{H};E]\ , \qquad (21)$$

with the summation limits specific for the PSS basis (see Tables I and II). The state capture cross sections were obtained from the corresponding state probabilities using Simpson-rule integration according to (18), with impact-parameter mesh and upper limit of 0.05 and 15.5 bohr, respectively. All trajectories in the close-coupling calculations began at $Z_0^-=-50$ bohr with the initial amplitudes (19b) and were terminated at $Z_0^+=400$ bohr.

Several interesting features stand out in Fig. 2. First, above $V_H\approx 0.2$ a.u. the small 4/1 (see Table II) basis becomes progressively deficient [Fig. 2, curve *a*] in describing the electron-capture reaction, accounting for about 30% of the cross section at $V_H=0.5$ a.u. as compared to approximately 75% accumulated by the same four helium ion states in calculations employing larger bases. This is a somewhat surprising result because experiments [27–33] indicate that the dominant transfer mechanism is $H(1s)\rightarrow He^+(n=2)$. What Fig. 2 suggest then is that, even though the total transfer into the higher shells of the helium ion is comparatively low ($\sim$25%) with respect to $He^+(n=2)$, higher adiabatic states are dynamically important. Notice that the cross section computed with the six orbitals dissociating to $He^+(n=3)$ included [Fig. 2, curve *b*], is much improved over the 4/1 curve, quantitatively and in the overall shape. The improvement attained by adding states corresponding to the next shell of He^+ (compare Fig. 2, curves *b* and *d* or *c* and *e*) is noticeable, yet it is by far smaller than the change resulting upon expanding the basis from 4/1 to 10/1 (compare Fig. 2, curves *a* and *b*). All the medium-size bases 10/1, 10/4,

TABLE II. The PSS basis sets employed in the present study. HeH^{2+} orbitals are referred to in the united-atom notation.

Label[a]	Size	Core[b]	$\{\psi^{He}\}$	$\{\psi^{H}\}$
4/1	5	none	$1s\sigma;3d\sigma;2s\sigma$ $2p\pi$	$2p\sigma$
10/1	11	4/1	$4f\sigma;3p\sigma;3s\sigma$ $3d\pi;3p\pi$ $3d\delta$	
20/1	21	10/1	$6h\sigma;5f\sigma;4p\sigma;4s\sigma$ $5g\pi;4d\pi;4p\pi$ $4f\delta;4d\delta$ $4f\phi$	
10/4	14	10/1		$5g\sigma;4d\sigma$ $4f\pi$
20/4	24	20/1		$5g\sigma;4d\sigma$ $4f\pi$
35/4	39	20/4	$7i\sigma;6g\sigma;5d\sigma;5p\sigma;5s\sigma$ $6h\pi;5f\pi;5d\pi;5p\pi$ $5g\delta;5f\delta;5d\delta$ $5g\phi;5f\phi$ $5g\gamma$	
10/10	20	10/4		$8j\sigma;7h\sigma;6f\sigma$ $7i\pi;6g\pi$ $6h\delta$
20/10	30	20/4		$8j\sigma;7h\sigma;6f\sigma$ $7i\pi;6g\pi$ $6h\delta$
35/10	45	35/4		$8j\sigma;7h\sigma;6f\sigma$ $7i\pi;6g\pi$ $6h\delta$

[a]The label notation is $\dim\{\psi^{He}\}/\dim\{\psi^{H}\}$.
[b]Basis is $\{\text{core}\}\oplus\{\psi^{He}\}\oplus\{\psi^{H}\}$.

TABLE III. Total cross section (in bohr^2) for $H(1s)+He^{2+}\rightarrow H^+ + He^+$ computed using the target propagator G_H with different PSS bases.

Basis[a]	V_H (a.u.) 0.1416	0.2003	0.3060	0.4006	0.4906
4/1	1.9294	4.8310	11.713	15.056	15.908
10/1	2.3391	6.5632	17.796	25.235	33.408
10/4	2.4184	7.1903	19.451	27.334	33.897
10/10	2.4242	7.2448	19.642	27.585	34.078
20/1	2.3809	6.7848	18.607	26.823	35.670
20/4	2.4629	7.4754	20.665	29.579	36.067
20/10	2.4691	7.5331	20.847	29.839	36.239
35/4	2.4945	7.6631	21.413	30.684	37.314
35/10	2.5012	7.7243	21.623	30.975	37.379
expt.[b]	1.1427	8.9277	24.926	35.175	41.424
	±0.3214	±0.8213	±1.786		

[a]See Table II.

[b]References [27] and [30] (including reported standard deviations).

20/1, and 20/4 provide a rather decent qualitative description of electron transfer until the ionization threshold is reached. Quantitatively, though, they fail to reproduce the cross section above $V_H=0.3$ a.u., becoming progressively worse with increasing velocity. The effect of including the adiabatic set dissociating to the hydrogen atom first-excited-shell states is pronounced as seen by comparing Fig. 2, curves *b* and *c* and curves *d* and *e*. Curiously, the resulting trend at the lower-velocity side is to increase the total transfer cross section,

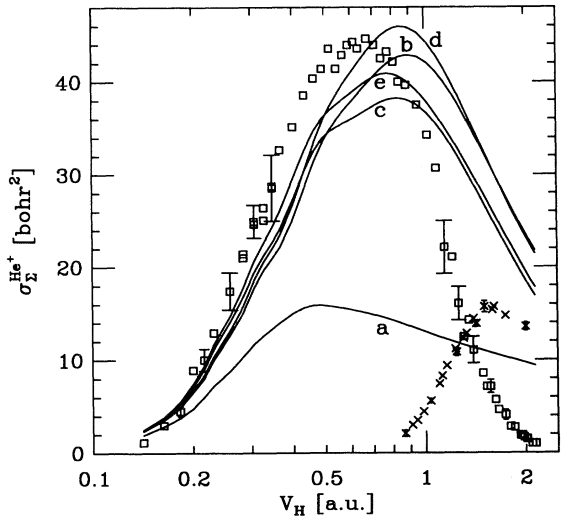

FIG. 2. Cross section for the electron-capture reaction $H(1s)+He^{2+}\rightarrow H^+ + He^+$ as a function of the target-projectile velocity. Single-channel PSS calculations with the target eikonal propagator G_H employing small and medium-size molecular-orbital sets (see Table II): curve *a*, 4/1; curve *b*, 10/1; curve *c*, 10/4; curve *d*, 20/1; curve *e*, 20/4. The experimental data (□) are from Shah and Gilbody [27] and Nutt *et al.* [30]. Also shown (×) for comparison is the measured ionization cross section $H(1s)+He^{2+}\rightarrow H^+ + He^{2+} + e^-$ taken from Shah and Gilbody [41] and Shah *et al.* [43]. Error bars at representative points reflect the reported statistical error. The relative systematic error in the charge-exchange measurements is estimated [27] to be 15%.

while after $V_H\approx 0.4$ a.u. the cross section is significantly reduced on adding the excited hydrogen atom states. The higher-velocity behavior is clearly more influenced by the target $H(n=2)$ related states than by the $He^+(n=3)$ capture subset. The charge-exchange cross section in the falloff wing typically decreases when adding excited hydrogen atom subsets, and increases with additional excited capture orbitals. Including more He^+-level subsets actually increases the transfer cross section in the entire reactive range, as is expected. But all these trends attenuate as the excitation level gets higher, indicating convergence with respect to the PSS basis (see also Fig. 3).

Figure 3 gives the collisional capture spectra up to $V_H=1$ a.u. obtained with a G_H defined over the PSS basis

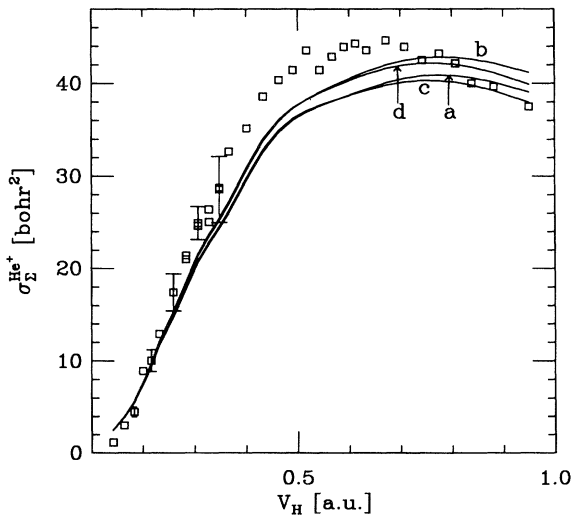

FIG. 3. Cross section for the electron-capture reaction $H(1s)+He^{2+}\rightarrow H^+ + He^+$ as a function of the target-projectile velocity. Single-channel PSS calculations with the target eikonal propagator G_H employing medium and large molecular orbital sets (see Table II): curve *a*, 20/4; curve *b*, 35/4; curve *c*, 20/10; curve *d*, 35/10. The measured charge-exchange points shown (□) are the same as in Fig. 2.

sets 20/4, 35/4, 20/10, and 35/10. A brief comparison with Fig. 2 hints that below ionization the 35/10 capture spectrum [Fig. 3, curve *d*] is close to a converged entrance-channel propagator calculation. Table III provides the measured [27,30] total charge-exchange cross section and the calculated results for nine adiabatic bases at five velocities in the range where a PSS model excluding functions representing the continuum is applicable. For $V_H=0.1416$ a.u. the semiclassical model overestimates by almost twice the small total cross section. But this point is in the buffer region separating quantal and semiclassical descriptions; a regime where quantum results seem to be distinctively lower (see Fig. 6 in Ref. [17]). At higher velocities the PSS cross sections are clearly below the experiment. A glance at any basis-set series of values in Table III, e.g., 10/10,20/10,35/10 or 20/1,20/4,20/10, should be convincing that further enlargement of the PSS basis would be unlikely to bridge over the discrepancy from measured transfer cross sections [27,30]. The problem lies with the target propagator, which provides an incomplete description of the collision as soon as significant electron probability is captured into the projectile (distorted) states [54].

Finally, we mention that the present results are qualitatively similar to those of Piacentini and Salin [1] or Winter and Lane [2] with comparable PSS bases. For example, at the target-projectile velocity of 0.284 a.u. with three and ten states these authors report total cross sections of 11.7 and 13.5 $bohr^2$, respectively. Our 4/1 and 10/1 results at the same velocity are 10.4 and 15.1 $bohr^2$. These differences may be partly because their smaller basis is limited to three states whereas the 4/1 basis contains the complete excited shell of He^+, and apparently also because the coupling operator of Winter and Lane [2] (and possibly of Piacentini and Salin [1]) is not the scattering momentum but rather the nuclear momentum with the electronic origin placed midway between the nuclei. The couplings by $-i\nabla_R$ are identical to those by $-i\nabla_H$ only when the proton is the electronic origin [54].

B. G_{He} calculations for $He^+(1s)+H^+ \rightarrow He^{2+}+H$

Trajectories simulating this collision were started at $Z_0^- = -35$ bohr with the initial amplitudes (19a) and ran till $Z_0^+ = 200$ bohr. State cross sections, obtained upon numerical integration of (18) with a mesh of 0.03 and an upper limit of 6 bohr, yield the total transfer cross section according to the basis-dependent summation (Tables I and II)

$$\sigma_\Sigma^H(E)=\sigma[H\leftarrow He^+(1s);E] = \sum_{n,m\in H}\sum_{l=|m|}^{n-1}\sigma[\phi_{n,l,m}^H \leftarrow \phi_{1s}^{He^+};E] . \quad (22)$$

Charge exchange in collisions of protons and ground-state helium ions is considerably weaker than the transfer process in collisions of hydrogen and α particles. The maximum transfer cross section is about 60 times smaller [27,39] (see Fig. 1) and it happens on less than one-third of the impact range [2,7,21]. This is because the proton projectile possesses half of the charge while the target electron is more tightly bound. However, the picture emerging from the G_{He} calculations still conveys patterns portrayed in the previous subsection. Table IV contains results evaluated for several bases at five velocities ranging from the transfer threshold to the onset of ionization. Total electron-transfer cross sections computed with the adiabatic bases 10/10, 20/10, 35/10, and 35/4 as a function of the target-projectile velocity are shown in Fig. 4 together with the experimental results for charge exchange [37–40] and ionization [40,42]. As seen from Table IV, the small 4/1 PSS basis calculations underestimate the charge-exchange cross section by more than 45%, worsening with increasing velocity like the 4/1 results in Sec. IV A. When the basis size increases, the PSS cross section slowly approaches the experimental curve from below. Clearly, target orbitals are more important

TABLE IV. Total cross sections (in $bohr^2$) for $He^+(1s)+H^+ \rightarrow He^{2+}+H$ computed using the target propagator G_{He} with different adiabatic bases.

	V_{He} (a.u.)				
Basis[a]	0.6410	0.7219	0.7754	0.8224	0.9092
4/1	0.0294	0.0649	0.0942	0.1196	0.1589
10/1	0.0410	0.0953	0.1466	0.1979	0.2968
10/4	0.0407	0.0944	0.1440	0.1922	0.2807
10/10	0.0410	0.0951	0.1451	0.1938	0.2831
20/4	0.0430	0.1007	0.1546	0.2077	0.3078
20/10	0.0430	0.1005	0.1540	0.2067	0.3054
35/4	0.0441	0.1040	0.1599	0.2154	0.3213
35/10	0.0444	0.1043	0.1605	0.2162	0.3224
expt.[b]	0.0553	0.1396	0.2225	0.2450	0.3828
	±0.0171	±0.0243	±0.0487	±0.0487	±0.0357

[a]See Table II.

[b]Reference [39] (including reported standard deviations).

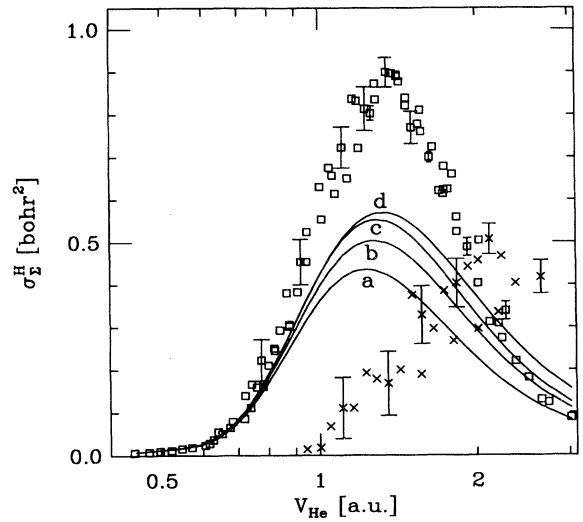

FIG. 4. Cross section for the electron-capture reaction $He^{2+}(1s)+H^+ \rightarrow He^{2+}+H$ as a function of the target projectile velocity. Single-channel PSS calculations with the target eikonal propagator G_{He} employing medium and large molecular orbital sets (see Table II): curve *a*, 10/10; curve *b*, 20/10; curve *c*, 35/10; curve *d*, 35/4. The experimental data (□) are from Peart, Grey, and Dolder [35]; Angel *et al.* [37]; Peart, Rinn, and Dolder [38]; Rinn, Melchert, and Salzborn [39]; Watts, Dunn, and Gilbody [40]. Also shown (×) for comparison is the measured ionization cross section of $He^{2+}(1s)+H^+ \rightarrow He^{2+}+H^++e^-$ taken from Watts, Dunn, and Gilbody [40] and Rinn *et al.* [42]. Error bars at representative points reflect the reported statistical error. The relative systematic error in the measurements varies between 7% and 14%.

to describe the rising wing (see Fig. 4) than capture states. In fact, below ionization the hydrogen atom ground state seems (Table IV) to be the dominant capture state almost exclusively [7,8,21], unlike the $H(1s)+He^{2+}$ collision where several capture orbitals are occupied [1–3,6,17,20,21]. At higher collision energies, though, more capture states become important as is demonstrated by the 35/10 and 35/4 cross-section curves above $V_{He} \approx 1$ a.u. (Fig. 4, curves *c* and *d*). Curiously, here as in Sec. IV A adding adiabatic states dissociating to hydrogen atom reduces the transfer cross section in the falloff wing. Similarly, enlarging the helium ion subspace generally increases the charge-exchange cross sections throughout the reactive range (see Figs. 2 and 4).

Up to $V_{He} \approx 1$ a.u., the total transfer cross section obtained with the 35/10 target propagator G_{He} agrees quite decently with the experimental values [39], falling either within the measurement error when V_{He} is under 0.7 a.u., or about 10% below the tolerance margin at somewhat higher velocities (Table IV). It is also evident from Table IV, as well as Fig. 4, that the 35/10 G_{He} PSS calculation can be further improved by including the next shell of degenerate helium ion orbitals, reducing the maximum deviation from experiment to about 5% in our estimation. The reason a target-propagator description below ionization is considerably better for a proton impinging on a ground-state helium ion than for the $H(1s)+He^{2+}$ collision is that here the overall charge exchange is much lower. As a result, throughout the collision G_{He} is almost identical with the full multichannel propagator (11) (see Sec. V E). It is also important to recognize that the onset of electron transfer in the collision of $He^+(1s)+H^+$ is already embedded in the ionization regime of the $H(1s)+He^{2+}$ collision. As such, a converged PSS model excluding continuum-representing functions will probably fall slightly short of the experimental transfer values in Table IV. Our reasoning is that the bound-state description omits a transfer mechanism of capture into and from the continuum. Figure 4 indeed illustrates that the ionization continuum is necessary to describe the entire collisional spectrum. Yet, even without continuum-representing functions, significant improvement may be achieved by expanding the adiabatic bound-state basis.

C. Projectile-propagator calculations

The situation described by the projectile (captured-electron) propagator is fundamentally different from a physical collision. In reality, the electron enters the collision while revolving about its nucleus in a definite atomic state, regardless of the relative velocity. The electron stays in this state until the collision forces begin to play at reasonably short distance [54]. But under the projectile-propagator description, the entrance dynamical state of the electron is not the atomic ground state, and is also dependent on the target-projectile velocity. This is because in the projectile Jacobi frame the electron must be traveling, i.e., it possesses average rectilinear momentum greater than zero. Within a finite basis, the initial state of the electron can be correctly described only in the Jacobi coordinates of the target [54]. For this reason alone we would expect the projectile-propagator results to deviate significantly from experiment. Indeed, transfer (as well as excitation) cross sections calculated using the captured-electron propagators grossly differ from experimental and the comparable target-propagator results. For instance, the $H(1s)+He^{2+} \rightarrow H^++He^+$ cross section at $V_H=0.4906$ a.u. is calculated using G_{He} to be about 170 bohr^2 which is over four times larger than the G_H value (Table III). The G_H transfer cross section for $He^+(1s)+H^+ \rightarrow He^{2+}+H$ is overestimated even more, e.g., ~ 6.9 bohr^2 at $V_{He}=0.7754$ a.u. as compared with 0.16 bohr^2 obtained in the G_{He} calculation (Table IV). The unreasonably high transfer cross sections predicted by the projectile-propagator model may be easily understood by noting that the dynamical entrance state (20) is not the ground state, but rather a superposition containing excited adiabatic states which are efficient charge-exchange mediators [63]. By the same token, the reactive impact-parameter range is much higher in the projectile-propagator calculations: 35 and 25 bohr for $H(1s)+He^{2+}$ and $He^+(1s)+H^+$, respectively. Similar values are found with target propagators when the initial atomic states are excited [63]. In conclusion, it is certain that collision simulations must begin with the target propagator.

V. MULTICHANNEL PROPAGATOR SIMULATIONS

Integration of the coupled equations (8) using the multichannel propagator (11) proceeds in a manner similar to the target-channel calculations (Sec. IV A), the only major difference being the evaluation of temporal propagator matrix elements. For every trajectory point Z, $\langle \psi_\alpha^m | G(Z,b,E) | \psi_\beta^n \rangle$ must now be computed according to (11) from the rearrangement probabilities at Z and the corresponding matrix elements of the single-channel propagators G_H and G_{He}. This procedure proved to be rather time consuming at low collision velocities, and here an alternative approximate matrix computation method may be employed. A trajectory Z grid made of positive and negative branches is constructed from the dynamical coupling R grid using the impact parameter b. Every point on this grid is then the beginning of an integration sector extending to the next higher Z grid point. The exact single-channel propagator matrices are given at the sector walls as these coincide with the coupling R grid. But the rearrangement probabilities are only known temporally, i.e., upon reaching the Z grid point during the actual integration. An approximate multichannel propagator matrix is obtained assuming that the rearrangement probabilities are constant throughout the sector, and equal to the probabilities at the sector starting Z coordinate. The multichannel propagator matrix is thus known on the sector boundaries, and anywhere between may be interpolated linearly. The precision of the propagator matrix evaluated in this way should increase with decreasing velocity because charge exchange is correspondingly diminishing. When the R grid is sufficiently dense this approximate integration procedure is reasonably accurate at low collision velocities. For example, with the present R grid of 239 points the error accumulated in the total charge-exchange and target-excitation cross sections is, respectively, 0.15% and 1.7% at the highest velocity where approximate integration has been performed (see Table V).

A. Electron capture in $H(1s)+He^{2+}$ collisions

The total electron-transfer cross section computed using the multichannel propagator for five PSS bases is depicted in Fig. 5 as a function of the relative velocity. All five theoretical curves essentially reproduce the experimental spectrum up to $V_H=0.3$ a.u. Above this velocity the prediction calculated using the smallest 10/4 basis (Table II) progressively worsens with increasing velocity [Fig. 5, curve a]. The four curves obtained with the larger adiabatic bases remain, however, faithful reproductions of the measured cross section till $V_H \approx 0.65$ a.u., which is slightly below the onset of ionization, after which they all overshoot the experimental results. The breakdown of the PSS model at this point is expected, since a strictly bound basis cannot fully account for ionization. Figure 5 clearly demonstrates convergence of the transfer cross section with respect to the adiabatic orbital basis in the regime where a PSS model excluding continuum-representing functions should indeed work. In particular, note the excellent agreement of the calculated 35/10 rising wing with the measured electron-capture spectrum [27,30]. Table VI provides the computed 35/10 multichannel total cross sections displayed in Fig. 5 and the corresponding level-selective components. The 35/10 electron transfer spectrum in the entire reactive range is also shown in Fig. 6 together with the target-propagator curve for the same PSS basis (Sec. IV A). It should be emphasized that in the velocity regime between 0.4 and 0.65 a.u. the multichannel propagator results for the bases 20/4, 20/10, 35/4, and 35/10 are all better than the nearly convergent 35/10 target-propagator transfer spectrum shown in Fig. 6.

It is instructive to compare the impact-parameter dependence (Fig. 7) of the charge-exchange cross section (i.e., the semiclassical partial cross section $2\pi Wb\,db$) computed using the multichannel propagator (solid lines) to that obtained from the target propagator G_H (broken lines) with the same adiabatic basis. At relatively low target-projectile velocity (Fig. 7, curves a), when overall

TABLE V. Comparison of cross sections from exact and approximate evaluation of the propagator matrix while integrating the coupled multichannel 35/10 PSS equations. $V_H=0.5424$ a.u. in $H(1s)+He^{2+}$ and $V_{He}=1.2301$ a.u. in $He^+(1s)+H^+$.

	$H(1s)+He^{2+}$		$He^+(1s)+H^+$	
	Exact	Approximate	Exact	Approximate
σ_Σ^{He}	42.9784	43.0368	0.7451	0.7434
σ_{1s}^{He}	0.2400	0.2414		
$\sigma_{n=2}^{He}$	31.4424	31.5116	0.4793	0.4783
$\sigma_{n=3}^{He}$	7.8931	7.8855	0.1155	0.1149
$\sigma_{n=4}^{He}$	2.3990	2.3929	0.0571	0.0573
$\sigma_{n=5}^{He}$	1.0040	1.0054	0.0932	0.0929
σ_Σ^H	2.8800	2.8315	0.5836	0.5842
σ_{1s}^H			0.4046	0.4049
$\sigma_{n=2}^H$	2.2307	2.1924	0.1300	0.1303
$\sigma_{n=3}^H$	0.6493	0.6391	0.0490	0.0490

electron transfer is still marginal, the single- and multichannel partial cross-section functions are almost identical, and as expected from the weighted formula (11), noticeable discrepancies occur primarily around the charge-exchange peaks. A manifestly different situation is observed at the higher collision velocity (Fig. 7, curves *b*), where the total capture cross section is near its maximum [Fig. 1, curve *a*]. Here the target-propagator partial cross section is significantly lower than the multichannel curve from $b \approx 0.8$ to about 6.5 bohr. This difference amounts to the better agreement of the multichannel-propagator total cross section with experiment. It should be pointed out, though, that in this range the target and the composite multichannel propagators are not really far apart (i.e., the G_{He} propagator quantitatively remains a small component).

The single- and the multichannel partial cross sections are practically equal above $b = 7.0$ bohr, even at the higher collision velocity (Fig. 7, curves *b*). The relatively large partial transfer cross section in this region is due to the high impact parameter [see (18)] while the capture probability is actually rather low, so the target dominates the multichannel propagator. At the impact-parameter range below 0.8 bohr, the near equality of the single- and multichannel partial cross sections is balanced in an opposite way. Here the transfer probability is in general high, so during the collision (11) evolves to be quite different from the target propagator G_{H}. Yet *b* is small, and the marked dispersion caused by probability transfer is largely suppressed, especially as charge-exchange probability usually decreases with *b* from its maximum at head-on impact.

B. Selective charge transfer from H(1*s*) to helium ion levels

With the 35/10 adiabatic basis, the transfer reaction $\mathrm{H}(1s)+\mathrm{He}^{2+} \rightarrow \mathrm{H}^{+}+\mathrm{He}^{+}$ is accurately described by the multichannel eikonal propagator (11) as long as ionization is negligible, i.e., when $V_{\mathrm{H}} \lesssim 0.65$ a.u. (see Fig. 5). In this range our results agree with the experimentally measured transfer cross sections [27,30] as well as with other theoretical calculations employing a semiclassical ETF approach [4–6,8–11,13,14,16–18,20–22]. From the rich pool of simulation data available we choose to compare (Fig. 5) the present results to relatively recent calculations of Errea *et al.* [21] and Fritsch [22] (tabulated in

TABLE VI. Total and level-selective charge-exchange cross sections (in bohr^2) as a function of the target-projectile velocity (in a.u.) in the $\mathrm{H}(1s)+\mathrm{He}^{2+}$ collision, computed using the multichannel PSS propagator with the 35/10 basis described in Table II.

V_{H}	$\sigma_{\Sigma}^{\mathrm{He}^+}$	$\sigma_{1s}^{\mathrm{He}^+}$	$\sigma_{n=2}^{\mathrm{He}^+}$	$\sigma_{n=3}^{\mathrm{He}^+}$	$\sigma_{n=4}^{\mathrm{He}^+}$	$\sigma_{n=5}^{\mathrm{He}^+}$
0.1416	2.5710	0.0025	2.4033	0.1494	0.0129	0.0028
0.1636	4.0644	0.0053	3.7942	0.2206	0.0365	0.0078
0.1828	5.7607	0.0096	5.1669	0.4856	0.0816	0.0172
0.2003	7.9558	0.0156	7.2628	0.5548	0.0997	0.0229
0.2164	10.0918	0.0220	9.1890	0.7213	0.1290	0.0305
0.2313	12.5689	0.0305	11.3319	1.0019	0.1622	0.0425
0.2586	15.6835	0.0450	13.7349	1.5796	0.2476	0.0766
0.2833	18.8339	0.0646	16.0705	2.2064	0.3808	0.1115
0.3060	21.9772	0.0848	18.4662	2.7651	0.5218	0.1393
0.3271	24.2276	0.1017	20.2342	3.1020	0.6263	0.1634
0.3469	26.1128	0.1171	21.7733	3.3009	0.7230	0.1987
0.3657	28.1470	0.1320	23.4245	3.5159	0.8278	0.2468
0.4006	32.5876	0.1580	26.8846	4.1004	1.0820	0.3626
0.4327	36.3949	0.1813	29.4591	4.9008	1.3363	0.5174
0.4626	39.0599	0.1958	30.7839	5.8151	1.5831	0.6820
0.4906	40.8005	0.2125	31.2744	6.6434	1.8502	0.8200
0.5172	42.0309	0.2274	31.4187	7.3386	2.1239	0.9223
0.5424	42.9784	0.2400	31.4424	7.8930	2.3990	1.0040
0.5665	43.8101	0.2685	31.4907	8.3025	2.6623	1.0861
0.5897	44.5723	0.2951	31.5761	8.5968	2.9220	1.1823
0.6119	45.2626	0.3276	31.6437	8.8090	3.1796	1.3027
0.6334	45.8726	0.3698	31.6865	8.9302	3.4410	1.4451
0.6713	46.8033	0.4517	31.7175	8.9988	3.9103	1.7249
0.7082	47.5639	0.5533	31.7243	8.9552	4.3310	2.0001
0.7423	48.0819	0.6730	31.5950	8.8924	4.6504	2.2711
0.7758	48.2537	0.8044	31.1705	8.7598	4.9428	2.5762
0.8070	48.0834	0.9463	30.4442	8.5986	5.1933	2.9010
0.8379	47.6764	1.0893	29.4951	8.4503	5.3868	3.2550
0.8815	46.8376	1.3190	27.9341	8.2120	5.5782	3.7943
0.9501	45.1377	1.6902	25.2982	7.7742	5.7349	4.6401

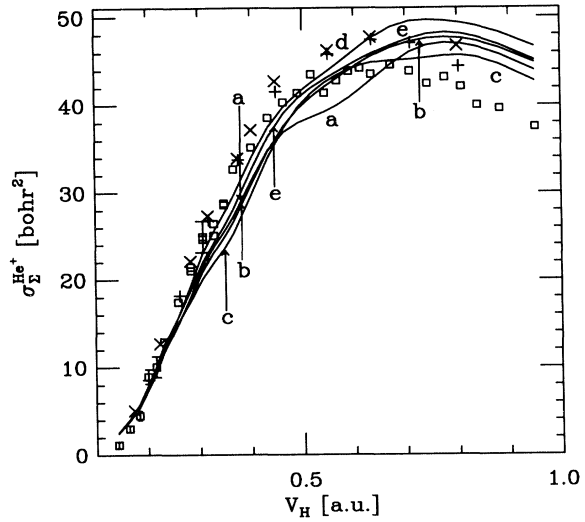

FIG. 5. Cross section for the electron-capture reaction $H(1s)+He^{2+}\rightarrow H^+ + He^+$ as a function of the target-projectile velocity, computed using the multichannel propagator with the following adiabatic bases (see Table II): curve *a*, 10/4; curve *b*, 20/4; curve *c*, 20/10; curve *d*, 35/4; curve *e*, 35/10. Displayed experimental data (□) are the same as in Fig. 3. Also shown are the results (×) of Errea *et al.* [21] obtained with a common molecular ETF and a PSS basis of ten states, and those (+) of Fritsch [22,32] employing a large atomic basis of 84 states modified by a plane-wave translation factor.

Ref. [32]), which also provide detailed level-selective cross sections. The former are PSS calculations with a basis of ten adiabatic states including a common translation factor that has been variationally optimized in a rather sophisticated manner [20,21]. Fritsch [22], on the other hand, expands the electronic wave function in a

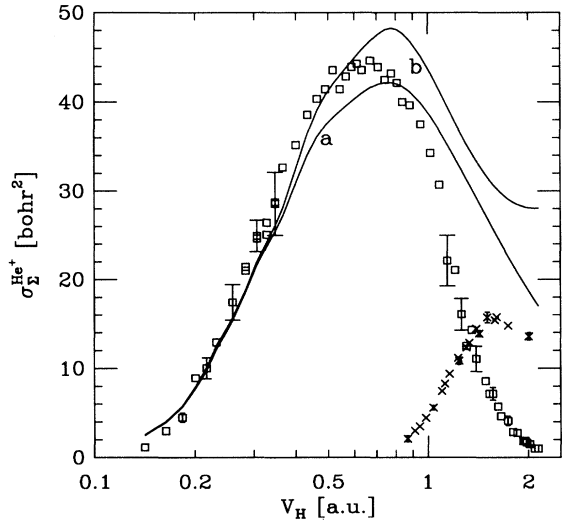

FIG. 6. Cross section for the electron capture reaction $H(1s)+He^{2+}\rightarrow H^+ + He^+$ as a function of the target-projectile velocity, computed with our largest PSS basis 35/10 (see Table II) using (curve *a*) the target propagator G_H; (curve *b*) the full multichannel propagator (11). Experimental capture (□) and ionization (×) cross sections are the same as in Fig. 2.

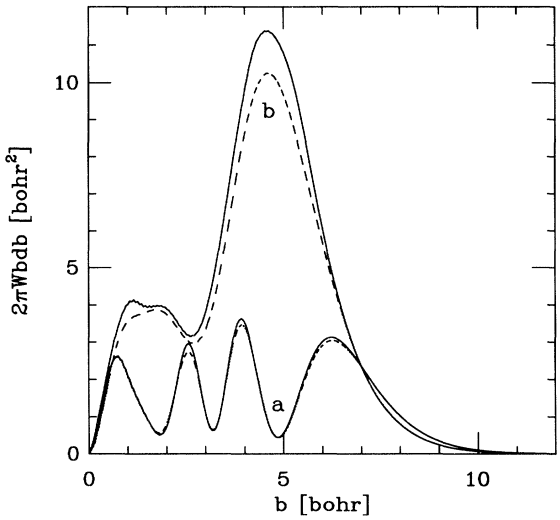

FIG. 7. The semiclassical partial cross section $2\pi Wb\,db$ for the charge-exchange reaction $H(1s)+He^{2+}\rightarrow H^+ + He^+$ as a function of the impact parameter *b*. Computations were performed with the 35/10 basis (see Table II) using the multichannel (solid line) and target (broken line) propagators when V_H equals (curve *a*) 0.2586 and (curve *b*) 0.5172 a.u.

large ETF-modified atomic basis comprising the lowest 84 states of helium ion, the $n=1,2$ states of hydrogen, and also the $n=2$ united-atom (Li^{2+}) states centered on the target. Although these two bases are quite different, they yield almost identical total and selective transfer cross sections in the region below ionization, and both (as do other ETF calculations quoted above but not shown in Fig. 5) essentially reproduce the total transfer experiment. However, while the cross section for helium ion production from the multichannel PSS simulations agrees closely with previous semiclassical translation-factor calculations, there is a wide discrepancy when selective capture into the He^+ levels is concerned.

Figures 8 and 9 juxtapose multichannel propagator cross sections for transfer into the levels $n=2$ and 3 of He^+ against the corresponding results of Errea *et al.* [21] and Fritsch [22,32]. In Fig. 10 we compare the calculations of Fritsch [22,32] and ours for the $He^+(n=4)$ capture. At $V_H=0.5$ a.u. the $n=2$ capture cross section (Fig. 8) computed with ETF methods is higher than obtained using the multichannel propagator (11) by more than 10 bohr^2, i.e., about 33%. This holds regardless of the adiabatic basis employed (Table II), for at the velocity in question the five calculated cross sections shown in Fig. 8 are no more than 2 bohr^2 apart. However, what in our calculation seems to be missing from the transfer into $He^+(n=2)$ appears as capture by higher excited levels of the helium ion, primarily $n=3$ and somewhat less $n=4$, for which the results of Errea *et al.* [21] and Fritsch [22,32] are considerably lower than the current calculation (see Figs. 9 and 10). Notice that, below $V_H\approx 0.2$ a.u., theirs and our $He^{2+}(n=2)$ capture cross sections are nearly the same, but then a gap begins to grow rapidly as the velocity increases. Evidently, translation-factor calculations and the multichannel propagator approach

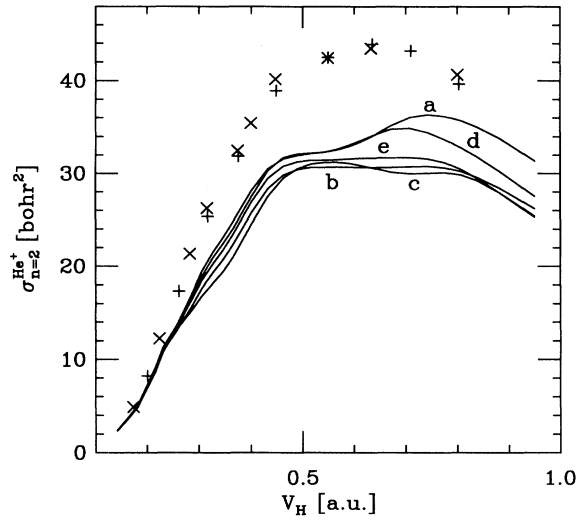

FIG. 8. Calculated multichannel-propagator cross section for the electron-capture reaction $H(1s)+He^{2+}\rightarrow H^+ + He^+(n=2)$ as a function of the target-projectile velocity. Legends refer to the PSS bases of Fig. 5. Also shown for comparison are results of other theoretical calculations: (×) Errea *et al.* [21]; (+) Fritsch [22,32].

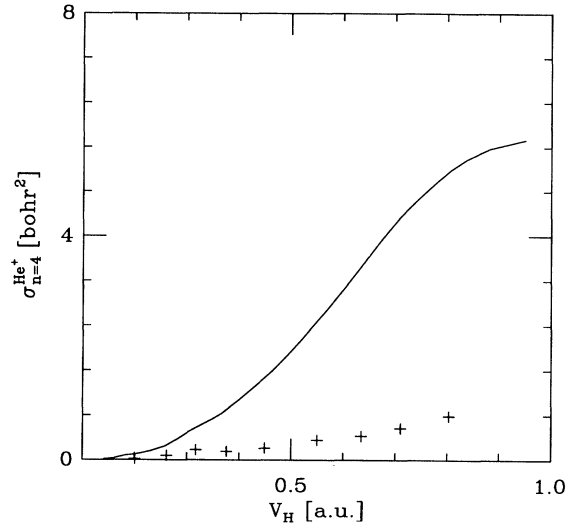

FIG. 10. Multichannel 35/10 PSS cross section for the selective electron capture $H(1s)+He^{2+}\rightarrow H^+ + He^+(n=4)$ as a function of the target-projectile velocity. See Fig. 8 for further details.

support different mechanisms for electron transfer in slow $H(1s)+He^{2+}$ collisions.

The multichannel PSS results (see Table VI and Figs. 8–10) suggest that excited capture as well as target states lying above the hydrogen atom ground level play a more prominent role in the transfer reaction than is currently believed [20–22,31,32,47]. Because the $n=2$ states of the helium ion are accidentally degenerate with the initial hydrogen atom ground state, it seems conceivable that capture into these states should dominate the reaction. This

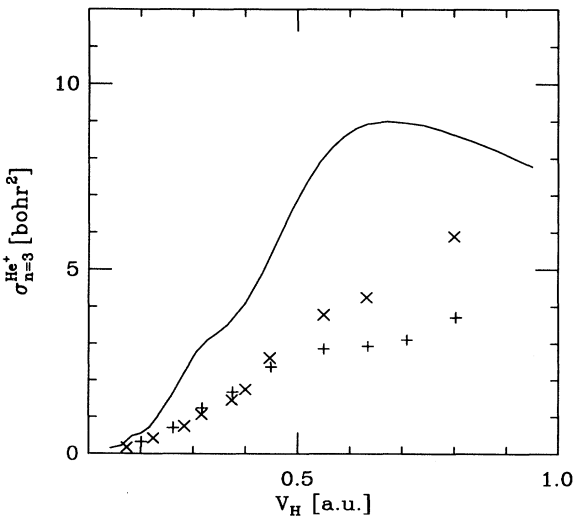

FIG. 9. Multichannel 35/10 PSS cross section for the selective electron capture $H(1s)+He^{2+}\rightarrow H^+ + He^+(n=3)$ as a function of the target-projectile velocity. See Fig. 8 for further details.

is indeed the case emerging from our simulations, but to a degree less than the ~95% according to calculations using the ETF [21,22]. Around $V_H=0.5$ a.u. (i.e., near the capture peak), the multichannel-propagator cross section into $He^+(n=2)$ amounts to about 75% of the total transfer. As can be seen from Fig. 8, the rising wing of the $n=2$ cross section is practically converged with respect to the size of the adiabatic basis, exhibiting maximum spread of ± 1 bohr^2 about the 35/10 profile [Fig. 8, curve *e*]. This fact is particularly illuminating, for all the bases employed in the multichannel PSS calculations depicted in Fig. 8 include the level $n=3$ of the helium ion. Without the adiabatic states corresponding to this excited shell the total transfer cross section is greatly reduced, and for $V_H > 0.3$ a.u. to an extent significantly below the selective $He^+(n=2)$ curves of Fig. 8.

The important role of the He^+ levels 3*s*, 3*p*, and 3*d* is already demonstrated by the target-propagator calculations shown in Fig. 2. Here, as in comparable multichannel simulations, the 4/1 PSS capture cross section (Fig. 2, curve *a*) is considerably smaller than the cross sections obtained when the basis contains the adiabatic states dissociating to the shell $He^+(n=3)$. In fact, the transfer enhancement induced on account of the adiabatic states corresponding to $He^+(n=3)$ is greater than what is revealed by the final ~15% of capture probability disposed into this helium ion level. The transfer role of this set of six adiabatic states is largely as dynamical mediators during the wave-function evolution in the reactive region. This happens because, at short range, molecular orbitals dissociating to the $He^+(n=3)$ shell, like $4f\sigma$ and $3s\sigma$, couple strongly by the collision momentum to the entrance adiabatic state $2p\sigma$ and to states from the set $He^+(n=2)$. This mediation is somewhat obscured when the associated dynamical couplings are modified due to a translation factor. The orbitals 3*s*, 3*p*, and 3*d* of the heli-

um ion indeed exhibit permanent asymptotic couplings with lower levels. Modifying the $He^+(n=3)$ capture states by an ETF so as to eliminate these residual interactions also changes their overall coupling. Particularly affected are the charge-exchange elements with the entrance state $2p\sigma$ and couplings to lower helium ion states (see, e.g., Figs. 10–13 in Ref. [6]). Coupling modification is generally more pronounced for the $n=3$ than for the $n=2$ states, which thus explains the diminished transfer role of the former level in translation-factor calculations. For example, even small ETF-modified PSS bases comparable to the 4/1 basis of Table II yield large charge-exchange cross sections that are often higher than the experiment [6,21]. Consequently, inclusion of the $He^+(n=3)$ set [21] likely acts to reduce the PSS + ETF capture cross section, thereby leading to attenuated final transfer to these states as compared with our results (Fig. 9).

C. Lyman and Balmer emissions of He II following $H(1s)+He^{2+}$ collisions

With the advent of ECR multicharged ion sources and the introduction of sensitive optical equipment in the vuv range, it became possible thanks to innovative design [31,64–66] to measure (n,l) selective emission lines following ion-atom collisions. The first measurements [27,28,30] of the Lyman α line when a charge-exchange $He^+(2s)$ metastable state is quenched by an electric field were in fact reported twenty years ago, and for long remained the only available selective data against which theory could be tested. Here controversy seems to have emerged because the $He^+(2s)$ capture cross sections of Shah and Gilbody [27] and Nutt *et al.* [30] are generally lower than the predictions of semiclassical theories, especially near the beginning of the peak transfer plateau where the discrepancy reaches a maximum of ~ 2 bohr^2. Since semiclassical calculations fare much better regarding the total capture cross section, it has been suggested by theorists [21,22,47] as well as experimenters [32], that the aforementioned measured $2s$ data [27,30] should be revised to be approximately 10–15 % higher. However, the difference between the measured total and the disputed $2s$ capture cross sections [27,30] is, considering the experimental error, in agreement with the sum of all Lyman emissions in the absence of electric field estimated from the recent data of Ćirić *et al.* [31] and Hoekstra, de Heer, and Morgenstern [32].

When discussing spontaneous emission following ion-atom collisions, one is reminded that the reactive stage of electron transfer and excitation from ground-state atoms is in fact short ranged. In our simulations, propagating 400 bohr (~ 2 μm) after the collision turning point (at $Z=0$) proved sufficient to extract constant final-inertial-state probabilities [54]. The slowest reactive event we have studied terminates after less than 0.1 ps, whereas the least metastable level of He^+ (i.e., $2p$) lives approximately 0.1 ns, that is, a thousand times longer. What this means is that as far as spontaneous photon emission is concerned, the collision prepares in a sudden way excited hydrogen and helium ion wave packets that (independently) evolve and emit over their respective excited nanosecond lifetimes. A nonelastic ion-atom collision experiment is therefore a two-stage process, short-time (sudden) reactive "product preparation" followed by a long "detection" phase of nonstationary product fluorescence. As such, it is clear that any comparison of theoretical capture cross sections to fluorescence data must be carried out with care to account for product emission dynamics, which may involve optical interference effects [67–70].

As a simple illustration of how emission interferences can arise, consider the QED expression (in atomic units) for the signal intensity detected at time t due to photons of wave number k and polarization $\mathbf{e}$ emitted from a single atom prepared in excited nonstationary state by a laser pulse [67]

$$I(k,\mathbf{e},r,t)=\frac{k^4}{r^2}\sum_f \sum_{i,j} \chi_i \chi_j^* \langle f|\mathbf{e}\cdot\mathbf{d}|i\rangle\langle j|\mathbf{e}\cdot\mathbf{d}|f\rangle \times\theta\left[t-\frac{r}{c}\right] \times\exp\left[-(i\omega_{ij}+\Gamma_{ij})\left[t-\frac{r}{c}\right]\right] . \tag{23}$$

Here c is the speed of light, r is the nascent atom detector distance, $\mathbf{d}$ is the electric dipole operator of the atom, ω_{ij} is the Bohr frequency associated with the excited levels i and j, Γ_{ij} is the sum of the level decay rates, and θ is the Heaviside function, which is zero for $t<r/c$ and 1 for $t>r/c$. The inner double summation in (23) is over initial excited atom states and the outer summation covers final ground states reached after the atom emits a photon of wave number k and polarization $\mathbf{e}$. The coefficients $\{\chi_i\}$ of the initial laser-prepared single-atom packet determine if the signal (23) decays in time while exhibiting quantum beats [67–70] due to periodic oscillation among nondegenerate fluorescent levels. Considering such interferences, a particular fluorescence cross section which is proportional to the signal (23) integrated over time may not necessarily reflect the initial excitation probability into the fluorescent level. A similar, yet more complicated, situation surely happens when a single atom (or ion) is collisionally prepared (incoherently) in an excited nonstationary state. In this case the coefficients $\{\chi_i\}$ of the emitting single-atom packet are initially related to the final inertial amplitudes $\{\chi_\alpha\}$ [see (16)] via a Stark transformation. However, in a simplified description like formula (23) they would now have to be time dependent due to emission cascades. Moreover, photons of the same wavelength and polarization may be involved with transitions between distinctively different initial and final degenerate states, which may promote further interference effects in the detected signal.

With the $H(1s)+He^{2+}\rightarrow He^+ + H^+$ reaction, it may be feasible to perform a simulation of the ensuing emission dynamics and derive the theoretical signals, since the levels, lifetimes, and electric dipole moments of helium ion are analytically known [71]. For instance, at every impact parameter b the emission could be propagated far-

ther using a master equation for the density matrix [68–70]. This would yield the required signal as a function of time and the impact parameter, leading to a detected emission profile [31–33] upon integration over the relevant range of b [see (18)]. An emission simulation program, curious as it might be, is, however, outside the scope of this study. Presently we shall examine the experimental data [27,30–32] against theoretical atomic-level capture results given in Table VII and the corresponding estimated emission cross sections. Estimates of fluorescence cross sections have been computed while neglecting possible interferences and including cascade contributions according to known [71] branching ratios. As is shown below, whenever the collisional fluorescence line may comprise several transitions, the predicted interference-free emission differs from experiment. In calculating the fluorescence cross sections we have also accounted, when necessary, for the experimental polarization correction to perpendicular detection as discussed extensively in Ref. [32], and in such cases the computed magic-angle (i.e., isotropic) result is illustrated for comparison.

The simplest situation to analyze involves a Lyman emission which is built from degenerate atomic transitions having orthogonal polarization, like $1s \leftarrow np_z$ and $1s \leftarrow np_x$. They cannot appear as a mutual interference term in a signal like (23), leading us to expect fluorescence composed of nearly independent decays even with cascade contributions. Figures 11 and 12 portray the experimental cross sections [32] for the $1s \leftarrow 2p$, $1s \leftarrow 3p$, and $1s \leftarrow 4p$ transitions of He II produced in collision of He^{2+} on H, against our corresponding 35/10 theoretical reactive-capture (short-time) and estimated (including cascades) fluorescence (long-time) data. The polarization correction factor for perpendicular detection (solid lines in these figures) has been computed from the simulated transfer cross sections (Table VII) using the appropriate formula from Table A.1 of Ref. [32]. Note, though, that below the velocity of 0.5 a.u., all calculated perpendicular Lyman emissions are practically identical to the magic-angle estimations (broken lines). Figure 11 also shows the Lyman-α cross sections measured [27,30] by electric-field quenching of the metastable $He^+(2s)$ collision product and the theoretical predictions. For comparison, the figures include the selective charge-exchange cross sections calculated by Fritsch [22,32], as well as the $2s$ and $2p$ capture results (Fig. 11) of Errea *et al.* [21]. We first discuss the spontaneous Lyman-β and -γ emissions (Fig. 12).

Up to about $V_H = 0.45$ a.u. the multichannel PSS ap-

TABLE VII. Selective (n,l) charge-exchange cross sections as a function of the target-projectile velocity in the $H(1s)+He^{2+}$ collision (see Table VI for further details).

V_H	$\sigma_{2s}^{He^+}$	$\sigma_{2p}^{He^+}$	$\sigma_{3s}^{He^+}$	$\sigma_{3p}^{He^+}$	$\sigma_{3d}^{He^+}$	$\sigma_{4s}^{He^+}$	$\sigma_{4p}^{He^+}$	$\sigma_{4d}^{He^+}$	$\sigma_{4f}^{He^+}$
0.1416	0.4040	1.9993	0.0068	0.0391	0.1035	0.0002	0.0017	0.0057	0.0054
0.1636	0.8743	2.9199	0.0074	0.0356	0.1776	0.0007	0.0047	0.0141	0.0170
0.1828	1.0441	4.1227	0.0122	0.0615	0.4120	0.0030	0.0105	0.0306	0.0375
0.2003	1.3515	5.9113	0.0183	0.1043	0.4322	0.0027	0.0229	0.0326	0.0414
0.2164	1.9152	7.2738	0.0285	0.1693	0.5235	0.0088	0.0305	0.0469	0.0429
0.2313	2.7152	8.6167	0.0413	0.2598	0.7008	0.0127	0.0306	0.0655	0.0534
0.2586	3.0766	10.6582	0.0781	0.4028	1.0986	0.0118	0.0369	0.1046	0.0942
0.2833	3.3039	12.7666	0.1160	0.5563	1.5341	0.0172	0.0588	0.1784	0.1265
0.3060	3.7648	14.7014	0.1569	0.6792	1.9289	0.0138	0.0889	0.2552	0.1639
0.3271	4.1648	16.0693	0.1613	0.6952	2.2455	0.0106	0.0987	0.3201	0.1969
0.3469	4.6093	17.1640	0.1280	0.6546	2.5182	0.0153	0.1049	0.3719	0.2308
0.3657	5.1838	18.2407	0.0968	0.6279	2.7913	0.0210	0.1199	0.4197	0.2673
0.4006	6.5110	20.3736	0.0883	0.6782	3.3338	0.0222	0.1667	0.5370	0.3560
0.4327	7.5691	21.8899	0.1073	0.8423	3.9512	0.0202	0.2057	0.6322	0.4783
0.4626	8.1287	22.6553	0.1416	1.0587	4.6148	0.0272	0.2308	0.7048	0.6204
0.4906	8.2677	23.0067	0.1863	1.2624	5.1947	0.0404	0.2628	0.7939	0.7530
0.5172	8.2106	23.2082	0.2328	1.4222	5.6836	0.0572	0.3008	0.8994	0.8665
0.5424	8.0661	23.3763	0.2835	1.5577	6.0518	0.0766	0.3475	1.0303	0.9445
0.5665	7.9165	23.5742	0.3178	1.6415	6.3432	0.0989	0.3937	1.1828	0.9868
0.5897	7.7732	23.8029	0.3436	1.6960	6.5573	0.1239	0.4526	1.3533	0.9921
0.6119	7.6389	24.0048	0.3584	1.7323	6.7183	0.1532	0.5267	1.5342	0.9655
0.6334	7.5065	24.1800	0.3661	1.7642	6.8000	0.1839	0.6143	1.7207	0.9222
0.6713	7.2727	24.4448	0.3719	1.8259	6.8011	0.2366	0.7936	2.0532	0.8269
0.7082	7.0570	24.6673	0.3935	1.9146	6.6472	0.2752	0.9548	2.3594	0.7416
0.7423	6.8654	24.7296	0.4361	1.9988	6.4575	0.3041	1.0803	2.5708	0.6952
0.7758	6.6357	24.5348	0.4883	2.0837	6.1879	0.3282	1.1933	2.6982	0.7232
0.8070	6.3858	24.0584	0.5349	2.1570	5.9066	0.3485	1.2799	2.7744	0.7906
0.8379	6.1205	23.3745	0.5848	2.2272	5.6383	0.3721	1.3322	2.8226	0.8599
0.8815	5.7481	22.1861	0.6640	2.3153	5.2326	0.4149	1.3513	2.8702	0.9418
0.9501	5.1480	20.1502	0.7963	2.4446	4.5333	0.5021	1.3082	2.9061	1.0186

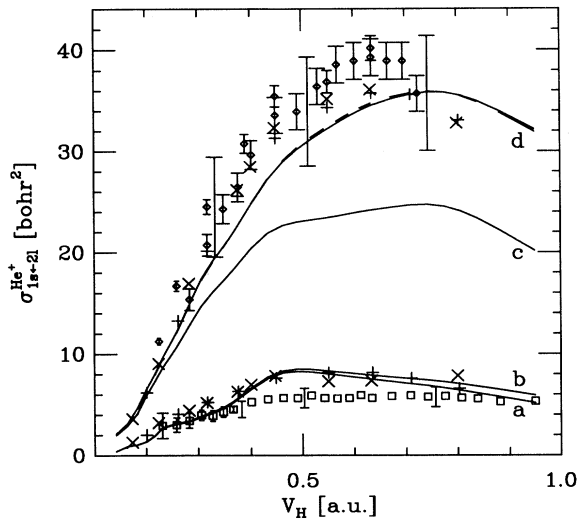

FIG. 11. Selective capture and emission cross sections for the $2s$ and $2p$ levels of the helium ion after collision of an α particle and hydrogen atom, displayed as a function of the target-projectile velocity. Multichannel-propagator results: curve *a*, the $2s$ capture cross section shortly after the reactive collision has ended, namely, when the internuclear distance reaches 400 bohr; curve *b*, the long-time (i.e., for R on the order of millimeters) $2s$ capture cross section including curve *a* and all contributions from emission cascades originating in levels higher than $2s$ (see text for details); curve *c*, same as curve *a* but for reactive capture into the $2p$ level of He^+; curve *d*, the calculated total (long-time) $2p$-$1s$ emission cross section which comprises curve *c* and the cascades ending in the $2p$ level (the solid line is the emission perpendicular to the beam including a polarization correction described in the text, while the broken line is the isotropic emission). Other theoretical short-time capture cross sections: (×) Errea *et al.* [21]; (+) Fritsch [22,32]. Experimental data: (□) the (long-time) $2s$ capture cross section measured by Shah and Gilbody [27]; (◇) the $He^+(1s\leftarrow 2p)$ emission cross section taken from Ćirić *et al.* [31] and Hoekstra, de Heer, and Morgenstern [32]. Error bars usually reflect the statistical error unless they appear without a point, when they equal the root-mean-square total (statistical and systematic) error of the measurement to the left.

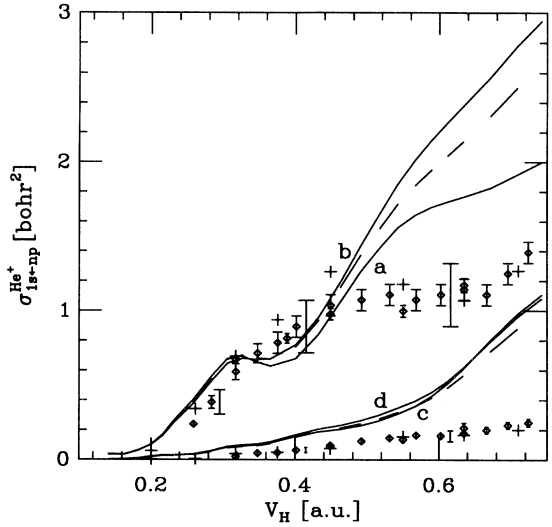

FIG. 12. Selective capture and emission cross sections for the $3p$ and $4p$ levels of He^+ after collision of an α particle and hydrogen atom, displayed as a function of the target-projectile velocity. Multichannel-propagator results: curve *a*, the $3p$ reactive (short-time) capture cross section; curve *b*, the long-time (including cascades from levels higher than $3p$) perpendicular polarization corrected (solid line) and uncorrected (broken line) $3p$-$1s$ emission cross section; curves *c* and *d* are, respectively, like curves *a* and *b* but for the level $4p$ of the helium ion. Selective charge-exchange cross sections calculated by Fritsch [22,32] are depicted by (+) and the experimental perpendicular emission data (◇) are from Ćirić *et al.* [31] and Hoekstra, de Heer, and Morgenstern [32] (error legends as in Fig. 11).

proximation (Fig. 12, curve *b*) to the $1s\leftarrow 3p$ line is in decent agreement with the data measured perpendicular to the ion beam. Our calculated $1s\leftarrow 4p$ emission (Fig. 12, curve *d*) is not as good as the $1s\leftarrow 3p$ prediction. Yet the discrepancy from the rather low experimental cross section is much smaller than the difference between the multichannel PSS simulations and the atomic ETF results of Fritsch [22,32] for selective $n=4$ capture (see Fig. 10). Given the marked disagreement between multichannel PSS level cross sections and other theoretical computations (see Figs. 8–10), it is more than interesting to note that, for selective capture into $3p$ under $V_H \approx 0.5$ a.u., the cross section of Fritsch [22] is roughly the same as ours (Fig. 12, curve *a*). It is definitely lower above this velocity. Also, his $4p$ charge-exchange prediction is always under the 35/10 multichannel PSS curve (Fig. 12, curve *c*). Fritsch [22] includes two more helium ion shells in his calculations, which might indicate a deficiency of the 35/10 adiabatic basis concerning capture into $4p$ and perhaps $3p$ at higher collision velocities. But high 35/10 cross sections above $V_H=0.5$ a.u. may also be due to the nearing onset of ionization, which is altogether excluded from the present treatment.

The proximity (in absolute magnitude) of the estimated 35/10 emissions (Fig. 12, curves *b* and *d*) to the measured Lyman lines below ionization, and the excellent reproduction of the total capture cross section over that range (see Fig. 5, curve *e*), both imply agreement with experiment for the combined field-free and electric-field-induced Lyman-α fluorescence from the product helium ion. Indeed, the multichannel PSS emission of $2p$ estimated while including repopulation by cascades from higher levels (Fig. 11, curve *d*), is at most 10–12 % lower than the experimental data. This is actually quite reasonable agreement considering that the reactive transfer curve *c* in Fig. 11 is by far more diminished. Radiative higher-level branching ratios favor $2p$ repopulation over $2s$ [71], so that the calculated selective cross sections for $2s$ capture and electric-field quenching are rather close (Fig. 11, curves *a* and *b*). Both are larger than the measured data [27,30] above the velocity of 0.3 a.u. In fact, the predicted excess $2s$ cross section approximately compensates the deficiency in our theoretical $2p$ emission. For example, at $V_H \approx 0.5$ a.u. the calculated $2s$ and $2p$ emissions differ with alternating sign by roughly 3.0 bohr^2 from the experimental spectra. Observe that ETF

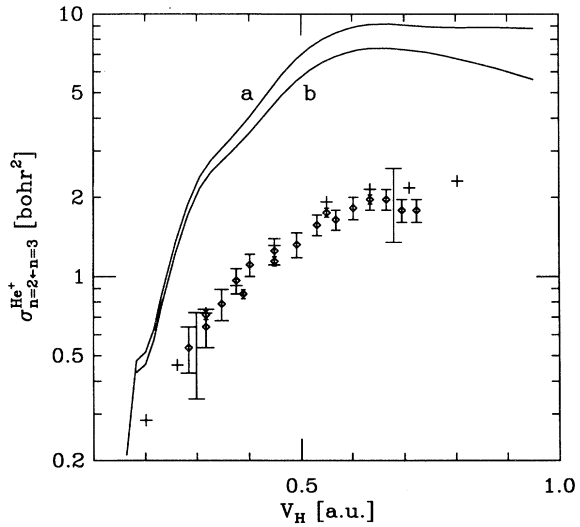

FIG. 13. The He II Balmer-α emission cross section recorded following a collision of He^{2+} on H(1s) as a function of the target-projectile velocity. The solid lines are the multichannel PSS profiles including (curve a) and excluding (curve b) cascades from levels $n=4$ and 5. Also shown (+) is the emission profile similarly computed using the capture results of Fritsch [22,32]. The experimental cross sections (◇) are taken from Ćirić *et al.* [31] and Hoekstra, de Heer, and Morgenstern [32] (error legends as in Fig. 11).

calculations [21,22] and multichannel PSS simulations yield similar cross sections for reactive transfer into the 2s level, but are significantly far apart regarding the 2p capture. The reason is probably the translation-factor modification of basis states. Since the 2p level exhibits dynamical asymptotic couplings with many more orbitals than 2s (e.g., 1s, 3s, and states from 3d as compared with the 3p coupling to 2s), it clearly must be more susceptible to the ETF incorporation. Note that calculations with translation factors give a 2p capture curve that is very close to the measured Lyman-α cross section [32]. Thus, combined with their generally larger result for transfer into 2s, the total ETF charge-exchange prediction is somewhat higher than ours as well as higher than the experiment (see Fig. 5).

When cascade contributions are included in the theoretical 2p emission, the 35/10 multichannel PSS level transfer mechanism described by Figs. 8 curve e, 9, and 10 is rather acceptable, especially since what seems to be missing from the 2p fluorescence turns out to be an excessive prediction for a metastable $He^+(2s)$ product, an indication, in our opinion, of optical interference effects during the radiative stage. But we shall postpone discussing any such interference to future work [72], and presently focus attention on the Balmer-α line. It is perhaps the most important emission with regard to the transfer mechanism emerging from our multichannel PSS simulations, predicting an $n=3$ capture cross section inherently (quantitatively and qualitatively) different from all other semiclassical theories [21,22]. Figure 13 then juxtaposes the experimental Balmer-α emission [31,32], which has been measured at the magic angle of 54.7°, together with emissions estimated from the 35/10 cross sections assuming independent (interference-free) decay with (curve a) and without (curve b) cascading contributions coming from higher levels. These estimations based on independently decaying levels are significantly higher than the measured data, and we must add here that similar theoretical predictions (Fig. 13) based on the ETF model of Fritsch [22,32] and possibly Errea *et al.* [21] are conversely in very good agreement [32] with experiment. Nonetheless, Fig. 13 is not at all contradictory to a transfer mechanism with a prominent $n=3$ role as portrayed by Figs. 8 and 9. Rather the opposite we feel should hold, because, as is argued below, Balmer-α emission following collisional preparation is likely to be infested with optical interference effects.

The Balmer-α line is composed [71] of unbranched transitions from the levels 3s and 3d to 2p, as well as 3p to 2s which funnels radiatively about 12% of the population residing at some point in the 3p level. Since multichannel PSS predictions to the 1s←3p emission below $V_H=0.5$ a.u. are accurate (Fig. 12), it seems reasonable that the discrepancy between our calculated Balmer-α line and the experiment (Fig. 13) originates from capture into 3s and 3d. Figure 14 compares the transfer into the levels 3s, 3p, and 3d computed for the 35/10 PSS basis using the multichannel propagator (11). The capture into $He^+(3d)$ absolutely dominates the 3s + 3d reaction (see Fig. 14, curves a and c), so that clearly the 2p←3d emission is the culprit behind our disagreement with the measured data [32]. Figure 14 also provides (broken lines) the detailed (state-selective) transfer cross sections into the 3d magnetic sublevels. Clearly, the transfer is distributed almost evenly between states 3d0 and 3d1, while

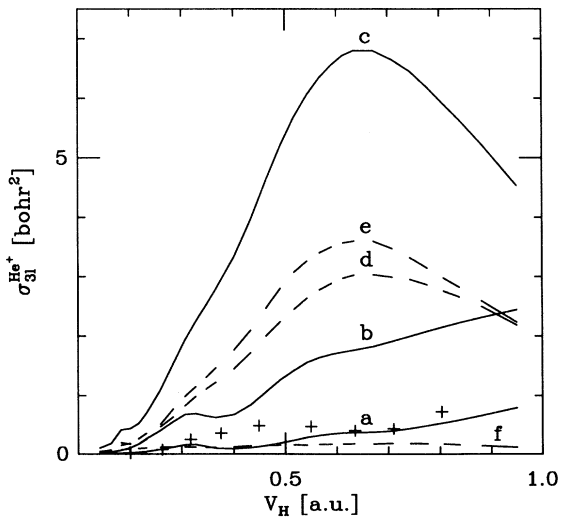

FIG. 14. Multichannel PSS cross sections for selective capture by the (3,l) levels of He^+ in H(1s)+He^{2+} collisions as a function of the relative velocity (solid lines): curve a, 3s; curve b, 3p; curve c, 3d. The broken lines are the breakup of the 3d capture into even magnetic states (3dm): curve d, 3d0; curve e, 3d1; curve f, 3d2. Also shown (+) are the 3s capture cross sections calculated by Fritsch [22,32].

$3d2$ remains practically passive. So to simplify the analysis we shall consider only emission coming from $3d1$ and $3d0$, although the real (transfer-induced) Balmer-α line would exhibit interference effects due to the small $2p1 \leftarrow 3d2$ component as well.

The two real even states $3d0$ and $3d1$ couple radiatively with perpendicular (in the $\hat{\mathbf{x}}$ direction) polarization to $2p1$ and $2p0$, respectively. As such, we immediately expect these Balmer-α emissions to interfere optically, if (as indeed is the case) the collisionally prepared wave function spans both $3d0$ and $3d1$. Neglecting cascade contributions (which from Fig. 13 are clearly not the source of the discrepancy), a detected signal [similar to (23)] from the $3d$ level along a single eikonal trajectory may be approximately proportional to

$$|\chi_{3d1}|^2|\langle 2p0|x|3d1\rangle|^2+|\chi_{3d0}|^2|\langle 2p1|x|3d0\rangle|^2 +(\chi_{3d0}\chi^*_{3d1}+\chi^*_{3d0}\chi_{3d1})\langle 2p0|x|3d1\rangle\langle 2p1|x|3d0\rangle \ . \tag{24}$$

The first two terms in the expression above are responsible for the independent emission cross section, Fig. 13, curve b. The third is an interference element that, depending on the sign of the real part of $\chi_{3d0}\chi^*_{3d1}$, would either amplify the detected transfer Balmer-α emission or attenuate it (the product $\langle 2p0|x|3d1\rangle\langle 2p1|x|3d0\rangle$ is negative [71]). In Fig. 15 we therefore plot against the impact parameter the partial cross sections $2\pi|\chi_{3d1}|^2b\,db$ and $2\pi|\chi_{3d0}|^2b\,db$ as well as the interference term $2\pi(\chi_{3d0}\chi^*_{3d1}+\chi^*_{3d0}\chi_{3d1})b\,db$, obtained for $V_H=0.4906$ a.u. from the 35/10 multichannel-propagator simulation. It is evident from the figure that the cross section for transfer Balmer-α emission may be influenced by optical interference. In fact, accounting only for the interference of the $3d1$ and $3d0$ emission should suppress the semiclassically predicted fluorescence by nearly 35%.

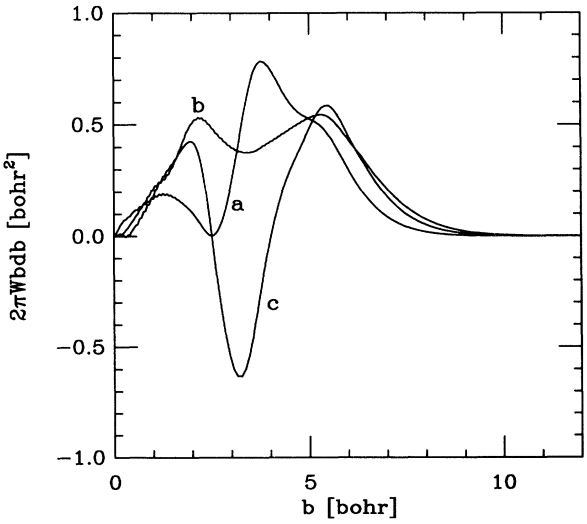

FIG. 15. Partial semiclassical cross sections associated with the Balmer-α $2p \leftarrow 3d$ transition of He^+ obtained from the reactive simulation data at $V_H=0.4906$ a.u.: curve a, $2\pi|\chi_{3d0}|^2b\,db$; curve b, $2\pi|\chi_{3d1}|^2b\,db$; curve c, $2\pi(\chi_{3d0}\chi^*_{3d1}+\chi^*_{3d0}\chi_{3d1})b\,db$.

Interestingly, the $3s$ capture curve a of Fig. 14 resembles closely the results of Fritsch [22,32], and below $V_H \approx 0.5$ a.u. the same is true for $3p$ capture (Fig. 12, curve a). The reason behind the vast difference separating the multichannel PSS $3d$ capture cross section, curve c of Fig. 14, from the calculation by Fritsch [22,32] and other theories [4–6,8–11,13,14,16–18,20] as well is precisely the translation factor. Observe that the helium ion $3d$ states exhibit residual asymptotic couplings with states from $He^+(2p)$ which is the dominant ($\sim 75\%$ by our estimation) capture level. Eliminating (unnecessarily) these couplings on introducing a translation factor modifies the $3d$-$2p$ couplings in the reactive region, and in effect shuts down probability transfer into $3d$. As a result, the $2p$-level capture efficiency is highlighted even more.

In conclusion, no meaningful relation between selective capture cross sections and the fluorescence from degenerate (n,l) levels of a system like the helium ion can be made without accounting for possible optical interferences. When the expected effect is small, say due to orthogonal polarization as in Lyman transitions, the multichannel PSS emission predicted while neglecting interference and adding higher-level cascade contributions is in good agreement with experiment. However, for complete understanding of the experimental results a dynamical fluorescence simulation is necessary. A more elaborate study of emissions induced by collisional electron transfer and including cascades is currently under way [72].

D. Hydrogen atom excitation in collisions with α particles

Collisional excitation of hydrogen atom is far less pronounced than electron capture by the doubly charged projectile. The two processes have nearby thresholds, and the reason for the higher charge-exchange productivity is effective capture [63] from excited hydrogen states. That is, hydrogen excitation serves as a doorway for charge transfer, so that collisional production of a final nascent hydrogen atom is greatly diminished. The excited hydrogen product becomes prominent only at high target-projectile velocities where the excitation current is large enough to survive depleting capture, i.e., ~ 1 a.u. and more. Ground-state ionization is abundant in this region but an excited hydrogen atom is relatively unaffected. That is because collisional ionization of the much diffused excited orbitals is considerably less effective than of a densely packed $1s$ ground state. Thus we would expect a rather decent description of hydrogen collisional excitation from the PSS model even in the ionization regime.

The multichannel PSS 20/10, 35/4, and 35/10 cross sections for the level-selective excitation process $H(1s)+He^{2+} \rightarrow H(n)+He^{2+}$ with $n=2$ and 3 are depicted against the collision velocity in Figs. 16 and 17. We focus attention in these figures on three regions of low, medium, and high velocity. Below $V_H \approx 0.55$ a.u. all multichannel PSS results shown are essentially converged, and so is the 20/4 cross section for the $n=2$ excitation which is missing from Fig. 16. The $n=2$ 10/4 calculation

(also not shown) soars after the velocity 0.2 a.u. and after that is increasingly higher than the rest. The $n=2$ excitation obtained with the 20/4 basis behaves the same shortly after $V_H=0.6$ a.u., yet remains under the 10/4 result. In the low-velocity region multichannel PSS cross sections are in excellent agreement with the previous calculations of Errea *et al.* [21] (Fig. 16) and Fritsch, Shingal, and Lin [73] (Figs. 16 and 17).

Across the intermediate-velocity regime, between 0.6 and 1 a.u., the cross sections computed with the bases 20/10 (curves *a* in Figs. 16 and 17) and 35/10 (curves *c* in Figs. 16 and 17) are reasonably close, albeit different. These two bases both contain the complete $n=2$ and 3 hydrogen shells (Table II). On the other hand, the $n=2$ excitation cross section (curve *b* in Fig. 16) computed with the 35/4 basis that excludes the $n=3$ shell is lower by approximately 1 bohr^2. Around $V_H=0.7$ a.u. the curves *a* and *b* in Fig. 16 show a shoulder structure that is absent altogether from the larger 35/10 basis calculation. In this velocity range the 35/10 multichannel PSS cross sections are fairly close to the ten-state PSS+ETF $n=2$ results of Errea *et al.* but in stark disagreement with the atomic calculations of Fritsch, Shingal, and Lin [73] which are much lower for both $n=2$ and 3 and feature prominent shoulders. Above $V_H=1$ a.u. the

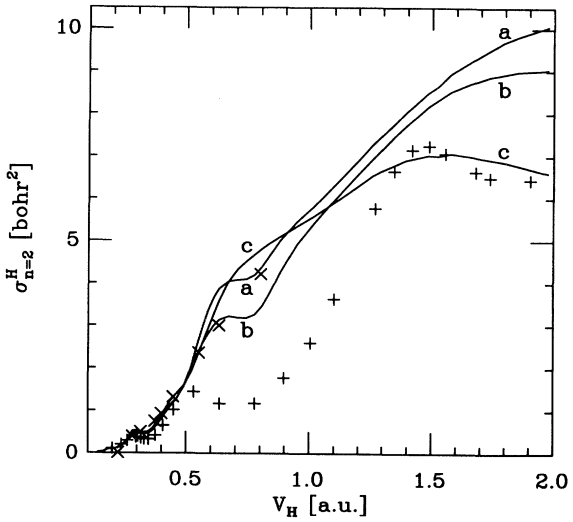

FIG. 16. Multichannel-propagator cross section for $n=2$ excitation of hydrogen atom by an α particle as a function of the collision velocity. Calculations (solid lines) employ the following adiabatic bases: curve *a*, 20/10; curve *b*, 35/4; curve *c*, 35/10. Other theoretical calculations shown for comparison: (×) Errea *et al.* [21]; (+) Fritsch, Shingal, and Lin [73].

TABLE VIII. Hydrogen selective (n,l) excitation cross sections as a function of the target-projectile velocity in the $H(1s)+He^{2+}$ collision (see Table VI for further details).

V_H	σ^H_{2s}	σ^H_{2p}	σ^H_{3s}	σ^H_{3p}	σ^H_{3d}
0.1416	0.0012	0.0152	0.0000	0.0004	0.0003
0.1828	0.0141	0.0795	0.0003	0.0023	0.0018
0.2164	0.0153	0.0993	0.0005	0.0058	0.0033
0.2586	0.0738	0.1762	0.0008	0.0162	0.0158
0.3060	0.0457	0.4715	0.0031	0.0353	0.0313
0.3469	0.0212	0.4835	0.0020	0.0417	0.0469
0.4006	0.0723	0.8100	0.0053	0.1070	0.0814
0.4626	0.1936	1.2086	0.0241	0.3214	0.1132
0.4906	0.1673	1.4222	0.0553	0.3372	0.1581
0.5172	0.1547	1.7052	0.0804	0.3101	0.2199
0.5424	0.1744	2.0563	0.0883	0.2707	0.2904
0.5897	0.2241	2.7307	0.0878	0.2306	0.3692
0.6119	0.2317	3.0518	0.1004	0.2271	0.3912
0.6334	0.2273	3.3585	0.1167	0.2335	0.4099
0.6713	0.2145	3.8260	0.1541	0.2840	0.4462
0.7082	0.2257	4.1058	0.1853	0.3922	0.4883
0.7423	0.2488	4.2596	0.2053	0.5105	0.5190
0.7758	0.2732	4.3926	0.2232	0.6207	0.5254
0.8070	0.3016	4.5117	0.2424	0.7286	0.5231
0.8379	0.3411	4.5990	0.2648	0.8425	0.5224
0.8815	0.4108	4.6905	0.3017	1.0113	0.5272
0.9501	0.5175	4.8289	0.3673	1.2628	0.5499
1.0181	0.6024	4.9815	0.4397	1.4587	0.5834
1.1419	0.7291	5.3410	0.5812	1.6592	0.6318
1.2562	0.8281	5.7097	0.6908	1.7408	0.6424
1.3486	0.8879	5.9059	0.7485	1.7778	0.6322
1.4855	0.9309	6.0994	0.7921	1.7752	0.6192
1.5772	0.9339	6.1404	0.8002	1.7476	0.6121
1.6537	0.9242	6.0879	0.7969	1.7189	0.6132
1.7953	0.8757	5.9962	0.7801	1.6806	0.6363
1.9761	0.7726	5.8436	0.7389	1.6859	0.7063

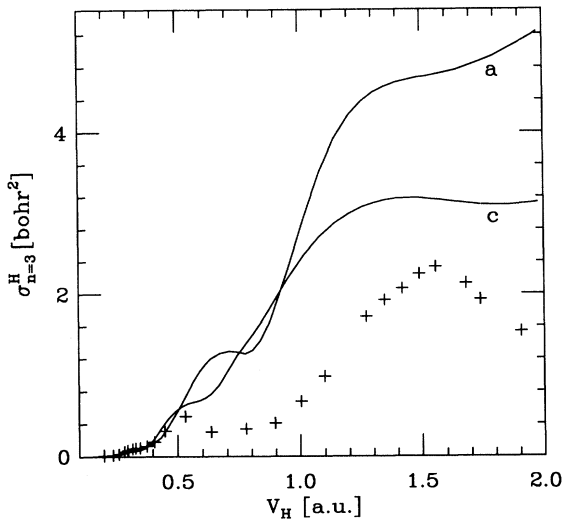

FIG. 17. Multichannel propagator cross section for $n=3$ excitation of hydrogen atom by an α particle as a function of the collision velocity (see Fig. 16 for explanation of legends).

20/10, 35/4, and 35/10 curves separate progressively as the velocity increases with the 35/10 result remaining the lowest. This indicates that for very fast collisions higher excited levels of hydrogen must be considered, and the 35/10 basis may be deficient even for high-velocity $n=3$ excitation.

Table VIII displays a sample from the simulated 35/10 cross sections for level-selective excitations of hydrogen atom by a passing α particle. Figures 18 and 19 portray,

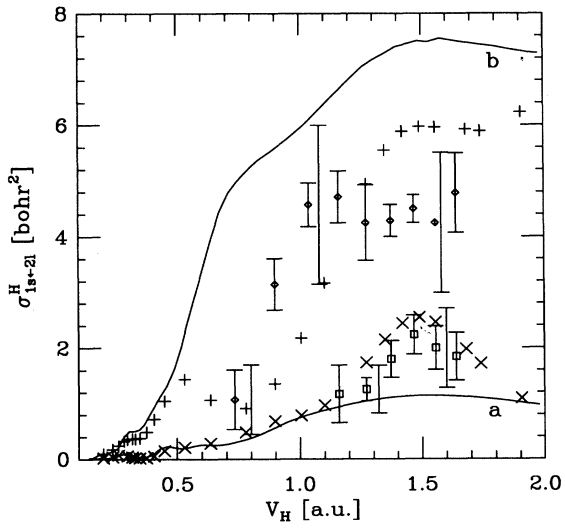

FIG. 18. Cross section for Lyman-α emission from hydrogen atom induced by a passing α particle as a function of the collision velocity. Multichannel-propagator 35/10 results including direct excitation and radiative cascades: curve *a*, the long-time emission from $2s$ in electric field; curve *b*, the field-free emission from the $2p$ level. The analogous $2s$ ($\times$) and $2p$ (+) emission cross sections are computed from the theoretical excitation data of Fritsch, Shingal, and Lin [73]. Experimental measurements (with error legends as in Fig. 11) quoted from Hughes, Geddes, and Gilbody [66]: (□) $2s$; (◇) $2p$.

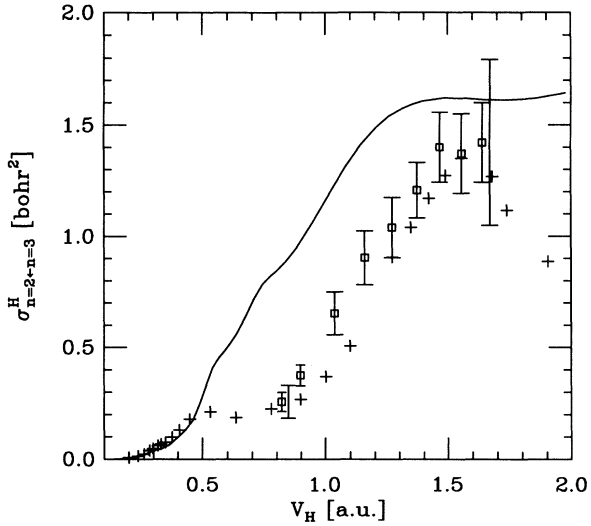

FIG. 19. The cross section for Balmer-α emission from hydrogen atom induced by a passing α particle as a function of the collision velocity. The 35/10 multichannel-propagator result includes direct excitation and radiative cascades. Also shown are emission cross sections calculated from the theoretical results (+) of Fritsch, Shingal, and Lin [73], and the measurements (□) of Donnelley, Geddes, and Gilbody [65] (see Fig. 11 for explanation of error legends).

respectively, the α Lyman and Balmer emissions computed from these level excitations, assuming interference-free decay and including cascades as in the previous subsection. For collision velocities under 0.55 a.u., the fluorescence spectra calculated from our 35/10 state-selective cross sections are again in excellent agreement with those similarly computed using the cross sections reported by Fritsch, Shingal, and Lin [73] (Figs. 18 and 19). However, at higher velocities a clear disparity exists between the theoretical predictions, except for the $2s$ emission induced by electric field in the intermediate range ($V_H \lesssim 1.1$ a.u.). The multichannel PSS calculations yield larger cross sections for the spontaneous Balmer-α (Fig. 19) and Lyman-α (Fig. 18, curve *b*) emissions and less structured spectra in fast collisions. Our results for these emissions are also higher from the experimental measurements of Donnelley, Geddes, and Gilbody [65] (Fig. 19) and those of Hughes, Geddes, and Gilbody [66] (Fig. 18). The maximum deviation of the estimated multichannel PSS Balmer-α emission from experiment is slightly less than 1 bohr^2, and it occurs in the middle of the intermediate-velocity range. The Balmer-α spectrum estimated in the same fashion using the results of Fritsch, Shingal, and Lin [73] is in much better agreement with the measured data [65]. It should be emphasized, though, that the theoretical spectra compared in Figs. 18 and 19 are computed while neglecting optical interference. But here, as in the case of the fluorescent transfer-product helium ion (Sec. V C), such effects are expected to be present and might attenuate the Balmer-α signal. Notice also that the multichannel PSS prediction for the electrically quenched $1s \leftarrow 2s$ and the spontaneous $1s \leftarrow 2p$ emissions are, respectively, lower (Fig. 18, curve *a*) and higher (Fig. 18, curve *b*) than the experimental cross sections [66].

E. Electron capture and target excitation in the collision of $He^+(1s)$ and H^+

We turn now to discuss the electron transfer reaction $He^+(1s)+H^+ \rightarrow He^{2+}+H$ portrayed in Fig. 20. Because capture from the tightly bound ground state of helium is generally small, the multichannel propagator (11) is almost identical to the target component G_{He} in nearly 80% of the rising wing of the transfer cross-section spectrum. Only around $V_{He}=1$ a.u. do the cross sections predicted for the 35/10 basis by the multichannel propagator (Fig. 20, curve *c*) and G_{He} (broken line in Fig. 20) begin to diverge visibly. From this point on the transfer reaction is clearly better described by the multichannel approach, especially across the transfer peak region, but also in the falloff wing. As mentioned in Sec. IV B, the total capture cross section is accurately reproduced by the 35/4 and 35/10 calculations (curves *b* and *c* in Fig. 20) up to $V_{He} \approx 0.9$ a.u., which in this collision system is slightly under the onset of ionization. Furthermore, for 85% of the pure capture regime the smaller 20/10 basis fares just as well. Note that with increasing basis size the multichannel PSS cross section approaches the experimental value from below. This trend persists far into the falloff wing until ionization becomes prevalent. There convergence patterns change, possibly because of a "wall effect" [22,47], as functions describing the continuum are not included in the PSS bases of Table II. Convergence from below toward the experimental value is peculiar to our unmodified (by ETF) adiabatic basis. Theoretical predictions from calculations performed with translation factors [4,7,8,11–13,15,19,21] usually approach the transfer cross section from above as seen in Fig. 20. They

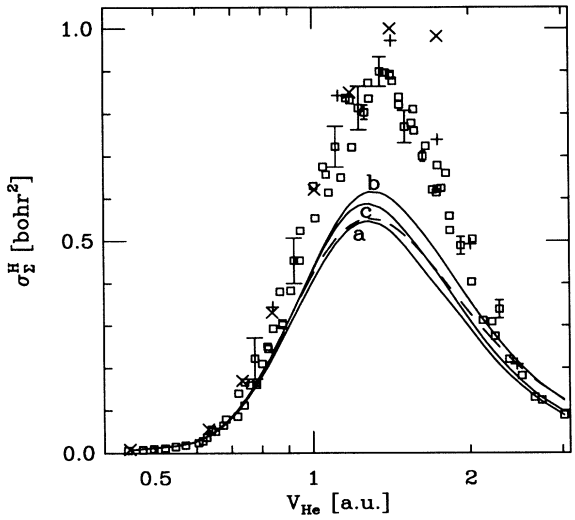

FIG. 20. Cross section for the electron-capture reaction $He^{2+}(1s)+H^+ \rightarrow He^{2+}+H$ as a function of the target-projectile velocity. Multichannel PSS calculations (solid lines) employing the following molecular basis sets (see Table II): curve *a*, 20/10; curve *b*, 35/4; curve *c*, 35/10. The superposed broken line is the 35/10 target-propagator G_{He} curve. Results of other semiclassical calculations with translation factors: (+) Winter [19] (Sturmian functions); (×) Errea *et al.* [21] (PSS). The experimental transfer data points (□) are the same as in Fig. 4.

thus fare better describing the peak of the capture spectrum [19,21], and even the falloff region [19] when the ETF-modified basis includes ionization functions. But for velocities below 0.9 a.u., the multichannel PSS description is comparably accurate. This is indeed the range where the bound adiabatic bases of Table II are (strictly) applicable.

For $V_{He} \gtrsim 0.9$ a.u. the 35/10 adiabatic basis insufficiently describes the charge-exchange reaction $He^+(1s)+H^+ \rightarrow He^{2+}+H$ because it lacks continuum-embedded functions as well as higher excited molecular orbitals from the target subspace $\{\psi^{He}\}$. In such violent collisions a transfer mechanism involving the recapture of an ionized electron should figure prominently in this weak reaction. This may be deduced from a microreversibility argument by considering the rather large cross section (as well as the lower threshold) for hydrogen ionization by an α particle [by the same token, ionization currents would not assist the (reverse) capture from $H(1s)$]. But a relatively high transfer current through the continuum only partly explains why the 35/4 and 35/10 peaks are ~33% shy of the experiment. The ability of a proton to capture the $He^+(1s)$ electron should also enhance on expanding the target subspace $\{\psi^{He}\}$, as demonstrated clearly by curves *a* and *b* in Fig. 20. That excited helium ion orbitals promote capture by a proton should not come as a surprise, because they participate, willingly, in the reverse reaction from ground-state hydrogen atom as evidenced by the emission experiments [27,30–33]. It is also well known [63] that charge exchange from a metastable $H(2s)$ state populates many more excited capture states of helium ion as compared to the $H(1s)$ case, but these are precisely the excited target states in the reaction considered here. Hence, as in the $H(1s)+He^{2+}$ collision (Sec. V A), excitation is a doorway for electron transfer. Ionization plausibly plays a similar doorway role in this system (but not in the reverse capture from hydrogen atom).

Figure 21 provides the calculated 35/10 PSS cross sections for level excitations of a helium ion by a proton projectile. Looking at Figs. 20 and 21 it becomes obvious that excitation is comparable to electron transfer, unlike when an α particle collides with hydrogen atom, where the magnitude of charge exchange greatly exceeds that of excitation. We would conceivably expect the efficiency of collisional target excitation to decrease with increasing principal quantum number. Indeed, this is what selective multichannel PSS cross sections reveal regarding excitation up to $n=4$ (curves *a*–*c* of Fig. 21). However, the $He^+(n=5)$ cross section (Fig. 21, curve *d*) is considerably larger than what might be anticipated from the excitation sequence $n=2$ to $n=4$. In our opinion this trend break indicates a deficiency of the 35/10 adiabatic basis. Using the convergence pattern of the multichannel PSS transfer cross section (Fig. 20), we estimate that augmenting the basis with the 21 orbitals corresponding to the next shell of helium ion states could increase by about 10–15 % both the calculated capture spectrum peak and the velocity limit to obtain excellent agreement with experiment. Additional excited orbitals from the target as well as the capture subsets are required for further improvement.

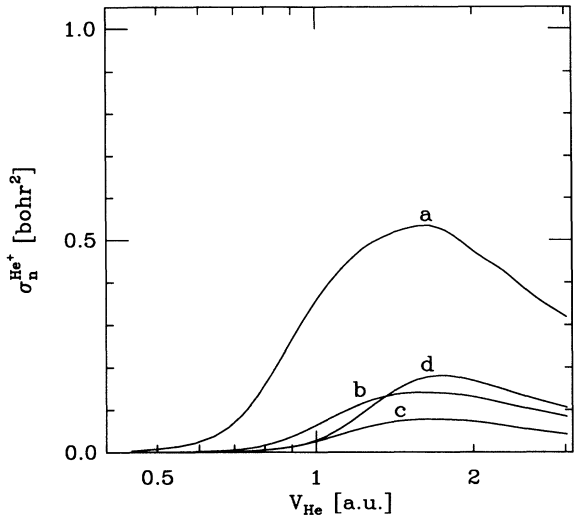

FIG. 21. Multichannel PSS (35/10 basis) cross sections for level excitation of a ground-state helium ion by a passing proton as a function of the relative velocity: curve *a*, $He^+(n=2) \leftarrow He^+(1s)$; curve *b*, $He^+(n=3) \leftarrow He^+(1s)$; curve *c*, $He^+(n=4) \leftarrow He^+(1s)$; curve *d*, $He^+(n=5) \leftarrow He^+(1s)$.

Nevertheless, they are probably not as crucial as would be functions representing (in a discrete sense [74]) the continuum manifold. As a matter of fact, semiclassical calculations with ETF-modified basis sets that do not model ionization fail at velocities approaching the falloff wing [21].

Capture promotion by excited target orbitals implies a transfer mechanism that extensively involves excited orbitals from the capture set $\{\psi^H\}$. The dominant charge-exchange component emerging from the multichannel PSS simulations (see Table IX and Fig. 22) is clearly the adiabatic orbital $2p\sigma$ that dissociates to ground-state hydrogen atom. Till $V_{He}=0.6$ a.u. it is almost solely responsible for the capture of the electron, but its reactive role progressively diminishes with increasing velocity. Thus near the transfer peak excited-state hydrogen already amounts to ~30% of the reaction products (see Table IX). Semiclassical calculations using ETF-modified bases [19,21] predict a qualitatively familiar picture for the rising wing and across the transfer peak while dissenting in the falloff regime (see Fig. 22). Quantitatively, however, H(1*s*) in translation-factor simulations generally summons a larger fraction from the transfer cross section. In fact, an ETF-modified hydrogen atom ground state remains the dominant capture orbital over the entire falloff wing [19]. Conversely, in our multichannel PSS scenario the importance of excited-state hydrogen atom continues to grow, reaching nearly half at collision velocities of about 1.7 a.u. Here it should also be stressed that the peak of the measured total cross section (Fig. 20) is actually shifted to higher velocity from the H(1*s*) capture maximum (Fig. 21). Figures 20 and 22 demonstrate together that the calculated total peak shifts in the right direction because of capture resulting in excited hydrogen atom as well as from promotion by excited helium ion.

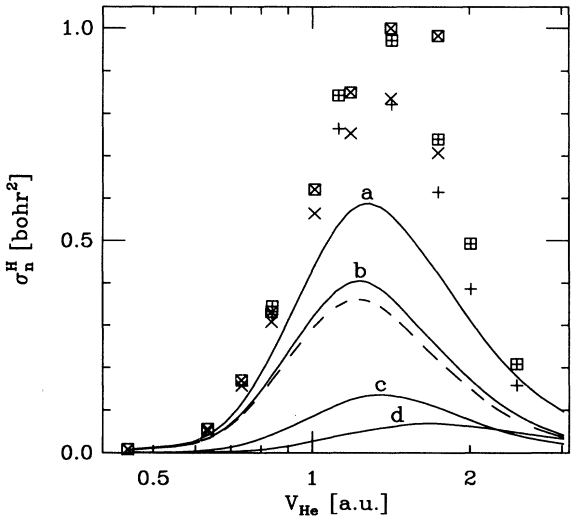

FIG. 22. Level breakup of the total 35/10 multichannel PSS cross section (curve *a*) for the transfer reaction $He^{2+}(1s)+H^+ \rightarrow He^{2+}+H$ as a function of the target-projectile velocity. Shown are the selective cross sections for capture into (curve *b*) H(1*s*); (curve *c*) H($n=2$); (curve *d*) H($n=3$). The broken line is the H(1*s*) capture spectrum computed with the smaller 20/10 basis. Other theoretical calculations provided for comparison: Winter [19], (+) for H(1*s*) and (⊠) for total transfer; Errea *et al.* [21], (×) for H(1*s*) and ⊠ for total transfer.

TABLE IX. Total and level-selective cross sections for charge exchange as a function of the target-projectile velocity in the $He^+(1s)+H^+$ collision (see Table VI for further details).

V_{He}	σ_Σ^H	σ_{1s}^H	$\sigma_{n=2}^H$	$\sigma_{n=3}^H$
0.4477	0.0072	0.0064	0.0006	0.0002
0.5483	0.0172	0.0149	0.0018	0.0006
0.5922	0.0255	0.0212	0.0033	0.0009
0.6410	0.0443	0.0362	0.0065	0.0016
0.7219	0.1034	0.0827	0.0170	0.0037
0.7754	0.1587	0.1253	0.0276	0.0059
0.8405	0.2364	0.1833	0.0431	0.0099
0.9092	0.3224	0.2450	0.0611	0.0163
0.9497	0.3719	0.2780	0.0724	0.0214
1.0060	0.4361	0.3217	0.0864	0.0279
1.0499	0.4802	0.3497	0.0977	0.0328
1.1102	0.5301	0.3801	0.1108	0.0392
1.1631	0.5617	0.3966	0.1211	0.0439
1.2301	0.5836	0.4046	0.1300	0.0490
1.2859	0.5876	0.3997	0.1345	0.0534
1.3505	0.5787	0.3851	0.1630	0.0575
1.3835	0.5699	0.3752	0.1354	0.0592
1.4280	0.5549	0.3599	0.1334	0.0615
1.5065	0.5229	0.3296	0.1279	0.0653
1.5717	0.4944	0.3044	0.1224	0.0676
1.6525	0.4591	0.2756	0.1146	0.0689
1.7682	0.4089	0.2384	0.1023	0.0682
1.8363	0.3796	0.2181	0.0948	0.0667
2.0170	0.3059	0.1689	0.0754	0.0616
2.2045	0.2428	0.1283	0.0583	0.0562
2.3794	0.1970	0.1000	0.0462	0.0508
2.6579	0.1424	0.0678	0.0324	0.0421
3.0197	0.0966	0.0420	0.0214	0.0332

As in the case of the projectile levels $n=3$ and 4 in the reverse reaction (Sec. V C), the reduced participation of excited hydrogen states predicted by previous theories [11–13,15,19,21], may be due to the change of their dynamical couplings with the hydrogen $1s$ orbital induced by the translation factor. This might mean that ETF calculations somewhat overestimate transfer efficiency into ground-state hydrogen. On the other hand, it is clear that enlarging the adiabatic basis beyond the 35/10 level (see Table II) must influence the capture probability distribution among hydrogen states. For instance, with 15 additional target states the maximum 35/10 cross section for selective $H(1s)$ capture (Fig. 22, curve *b*) is $\sim 10\%$ higher than the 20/10 result (broken curve in Fig. 22). Concerning the excited hydrogen levels the inverse is correspondingly true. Thus the multichannel-propagator calculation with the 35/10 basis conceivably underestimates the cross section for capture by $H(1s)$. It should also be mentioned here that continuum states couple dynamically more strongly to the denser $2p\sigma$ orbital than to diffuse hydrogen-related excited adiabatic functions. So inclusion of ionizationlike orbitals may facilitate transfer to the ground state by opening an additional possibility of recapturing the ionized electron from the continuum.

VI. SUMMARY AND DISCUSSION

The atomic-collision systems $H(1s)+He^{2+}$ and $H^+(1s)+H^+$ have been investigated within the framework of a translation-factor free semiclassical perturbed-stationary-state theory formulated in the preceding article [54]. The wave function of the electron evolving along a classical straight-line trajectory of the internuclear vector is expanded in a finite basis of (correctly dissociating) adiabatic orbitals of the HeH^{2+} molecule. Initially, before the collision begins, the electron occupies the adiabatic orbital that asymptotically becomes the $1s$ ground state of the target species. After the collision, when the nuclei are again far apart, the electron state is generally a superposition of adiabatic orbitals. The resulting expansion depends on the internuclear trajectory, and is obtained by solving a set of coupled first-order differential equations along a straight nuclear collision line. The coupling of adiabatic orbitals is furnished by the (Galilean invariant) scattering momenta of the charge-exchange rearrangements $H+He^{2+}$ and He^++H^+. We distinguish between single- and multichannel PSS theories [54]. In a single-channel formulation the couplings are due to the scattering momentum of one rearrangement. Each collision system may thus be "single channel," simulated by either a target (entrance-electron rearrangement) or a projectile (electron-capture rearrangement) propagator. The multichannel PSS propagator is composed of both the target and the projectile operators, and in a manner dictated by how much the temporal electron wave function actually spans the associated charge-exchange channels.

The invariant PSS formulation [54] admits asymptotic couplings as a necessary ingredient of a well-behaved atomic-collision theory. Residual couplings actually define the proper asymptotic scattering functions within the adiabatic basis employed [54,58]. These are precisely the eigenstates of the asymptotic propagator matrix, whose eigenvalues fix the traveling phases responsible for indeterminate propagated state capture probabilities [1,54]. Traveling phases emerge because a transferred electron is still described in a Jacobi frame suitable for the target. Such an electron must acquire asymptotic linear momentum reflecting its limiting rectilinear motion in the inappropriate Jacobi coordinates. A simple transformation, though, eliminates these traveling phases from the propagated amplitudes yielding the correct inertial-state capture probabilities. Interestingly, disregarding our asymptotic traveling transformation, a target-propagator theory is essentially the PSS model suggested long ago by Piacentini and Salin [1]. Implementing the traveling transformation makes a difference, nonetheless, in refining a theory strictly for total charge exchange to yield also state-selective cross sections. Notwithstanding, the target propagator by itself is not always enough to describe a collision.

The beauty of the PSS approach is that it provides a systematic manner of improving the approximation by expanding the basis of adiabatic molecular states. Several PSS bases comprising up to 45 bound adiabatic orbitals of HeH^{2+} have therefore been employed in our simulations. Below the collisional ionization threshold, total charge-exchange cross sections converge with respect to the basis size. A projectile propagator that inherently (and from the beginning) assumes the electron is already captured ill describes the collision, yielding grossly overestimated cross sections. Target propagators that take the electron to be always revolving around the target nucleus fare much better. For instance, in the case of $He^+(1s)+H^+\rightarrow He^{2+}+H$, up to about midway of the rising wing the calculated cross section is only slightly underestimated. But the target-propagator limit is definitely inferior to the experimental $H(1s)+He^{2+}\rightarrow H^++He^+$ cross sections. In contradistinction, for the two collision events studied here, the 35/10 multichannel PSS theory reproduces the total capture data measured below ionization. This is precisely because, unlike the rigid single-channel propagators, the multichannel evolution is governed by the temporal state of the electron. Note that for the $H(1s)+He^{2+}$ system charge exchange is a considerably more prevalent process than it is in $He^+(1s)+H^+$ collisions. Hence convergence of the former total cross section as the adiabatic basis increases in size is indeed conclusive indication that electron transfer reactions are correctly described within a multichannel PSS model. By the same token, target-propagator simulations ultimately must fall short. It should be realized that the multichannel propagator (11) is in essence the semiclassical PSS analogue of the full quantum Hamiltonian which determines the scattering wave functions in the collision systems $H(1s)+He^{2+}$ and $He^+(1s)+H^+$. Like the Hamiltonian, the effective PSS operator (11) is formally the same propagator for the two-electron rearrangements. However, as an effective operator [54] it is actually dependent on the collision conditions, namely, the initial state, the spatial nuclear tra-

jectory, and the relative velocity.

A bound adiabatic basis cannot describe a free electron, so such a PSS simulation ultimately must fail near the ionization threshold, and certainly above it. This is indeed the case emerging from the present calculations. In our opinion, this is a strong point in favor of the multichannel model, working where it should and failing where it should not. Nevertheless, the failure of bound-electron multichannel PSS simulations carried in the ionization regime is instructive, for they overestimate the falloff wing of the $H(1s)+He^{2+}\rightarrow H^{+}+He^{+}$ cross section while underestimating the peak of the $He^{+}(1s)+H^{+}\rightarrow He^{2+}+H$ curve. Both failed descriptions stem from basis-set deficiency, particularly the missing continuum manifold. In the collision of the α particle and hydrogen atom, the wave function of the electron undergoes drastic changes from being the hydrogen atom ground state. Above $V_H=0.8$ a.u., a large part of it represents not only capture but also ionization as evidenced by the ratios of the respective cross sections (see Fig. 2). Without any continuum-embedded basis states [19], ionization currents due to the strong collisional couplings are wrongly funneled ("wall effect") into the capture reaction whose cross section is thus increased. Adding basis functions representing continuum states [19,74] would likely temper this wall effect, thereby decreasing the capture cross section. On the other hand, when a proton collides with the tightly bound ground-state helium ion the situation is almost reversed. Here the electron wave function changes relatively little during the collision, resulting in a very small transfer component. Since the electric field of a proton is twice as weak as that of the α particle, charge exchange in this system competes heavily with target excitation, and in fact benefits from it (see Sec. V E). As such, including more excitation (and ionization) routes in the adiabatic basis would conceivably increase the predicted (yet underestimated) transfer cross section.

Below the ionization threshold, our 35/10 multichannel PSS calculations reproduce the experimental total charge-exchange cross section in the two collision systems $H(1s)+He^{2+}$ and $He^{+}(1s)+H^{+}$. In this regime, other semiclassical simulations [1–22] employing various forms of the translation factor perform equally well regarding the total transfer cross section while giving level-selective results different from the multichannel PSS theory. In $H(1s)+He^{2+}$ collisions, for instance, cross sections for transfer into excited helium ion levels higher than $n=2$ are manifestly larger in the multichannel PSS mechanism. Consequently, ETF-based theories apparently give a greater transfer role ($\sim 80\%$ at $V_H=0.5$ a.u.) to the principal participant $2p$ level than does ours ($\sim 60\%$). Yet the computed capture by the $2s$ level is actually comparable in the multichannel PSS and the translation-factor models (see Sec. V C). The reason behind the disagreement in charge-exchange cross sections involving the helium ion $n>2$ levels is the ETF modification of the associated excited states, which attenuates transfer current into them. A similar picture (and for the same reason) is observed in $He^{+}(1s)+H^{+}$ collisions. Here simulations with a translation factor emphasize more the capture by the hydrogen ground state as compared with the multichannel PSS calculations, the latter predicting significant participation also for excited hydrogen atom levels.

Despite stark differences from previous theories concerning level-selective charge exchange, the multichannel PSS theory prediction for the Lyman emissions of the helium ion following the capture from hydrogen atom is quite satisfactory when reckoning also the level repopulation from emission cascades. However, measured [32] charge-exchange-induced Balmer-α cross sections of He^{+} are suppressed with respect to our PSS calculations, with and without cascades. This result, albeit in disagreement with former theories, should not be too surprising, since the Balmer-α emission, which comprises several degenerate transitions of the same polarization, is highly susceptible to optical interference [67,69]. Indeed, an estimation assuming only a "double-slit Young" setup indicates that in a collisional preparation such interference may exist (see Fig. 15), and would most likely attenuate the detected emission signal. We wish to stress that ETF simulations too yield a collisionally mixed wave packet, and may thus lead to optical interference effects. Nonetheless, the latter are absent from any ensuing analysis [1–22] and/or the comparison with Balmer-α emission experiments.

This multichannel PSS study of the collision systems $H(1s)+He^{2+}$ and He^{+} $(1s)+H^{+}$ is far from being complete. Further investigation needs to be carried out in several directions. One is to simulate the emission dynamics following electron transfer in the collisions of the hydrogen atom and α particle below the ionization threshold. This venture should elucidate the magnitude of interference effects in the observed Balmer-α and -β fluorescence of the product helium ion [31–33] as well as from the hydrogen atom reactant [65,66]. It may also shed light on why the Lyman-α emissions of the helium ion predicted while including higher-level cascades differ slightly from experiment [27,31–33]. Work must be done to expand the PSS basis in the reactive simulations. Additional bound molecular orbitals are clearly required to further improve the description of the transfer reaction $He^{+}(1s)+H^{+}\rightarrow He^{2+}+H$. Even more important is to extend the theory toward the ionization regime, perhaps by including some discretized representation [19,74] of the electron continuum manifold.

ACKNOWLEDGMENTS

This research is made possible, in part, by NSF Grant No. CHE9307489. The author expresses his gratitude to Professor Karl F. Freed for his kind support. Useful discussions with Professor John C. Light are greatly appreciated.

[1] R. D. Piacentini and A. Salin, J. Phys. B **7**, 1666 (1974); **9**, 563 (1976); **10**, 1515 (1977).

[2] T. G. Winter and N. F. Lane, Phys. Rev. A **17**, 66 (1978).

[3] G. J. Hatton, N. F. Lane, and T. G. Winter, J. Phys. B **12**,

L571 (1979).
[4] B. H. Brandsen and C. J. Noble, Phys. Lett. **70A**, 404 (1979); J. Phys. B **14**, 1849 (1981).
[5] B. H. Brandsen, C. W. Newby, and C. J. Noble, J. Phys. B **13**, 4245 (1980).
[6] T. G. Winter and G. J. Hatton, Phys. Rev. A **21**, 793 (1980).
[7] T. G. Winter, G. J. Hatton, and N. F. Lane, Phys. Rev. A **22**, 930 (1980).
[8] M. Kimura and W. R. Thorson, Phys. Rev. A **24**, 3019 (1981).
[9] D. S. F. Crothers and N. R. Todd, J. Phys. B **14**, 2233; **14**, 2251 (1981).
[10] L. F. Errea, L. Méndez, and A. Riera, J. Phys. B **15**, 101 (1982).
[11] J. F. Reading, A. L. Ford, and R. L. Becker, J. Phys. B **15**, 625 (1982).
[12] T. G. Winter, Phys. Rev. A **25**, 697 (1982).
[13] W. Fritsch and C. D. Lin, J. Phys. B **15**, 1255 (1982).
[14] H. J. Lüdde and R. M. Dreizler, J. Phys. B **15**, 2713 (1982).
[15] B. H. Brandsen, C. J. Noble, and J. Chandler, J. Phys. B **16**, 4191 (1983).
[16] W. Fritsch and C. D. Lin, Phys. Rev. A **29**, 3039 (1984).
[17] M. C. van Hemert, E. F. van Dishoeck, J. A. van der Hart, and F. Koike, Phys. Rev. A **31**, 2227 (1985).
[18] C. W. Newby, J. Phys. B **18**, 1781 (1985).
[19] T. G. Winter, Phys. Rev. A **33**, 3842 (1986); **35**, 3799 (1987).
[20] L. F. Errea, J. M. Gómez-Llorente, L. Méndez, and A. Riera, Phys. Rev. A **32**, 2158 (1985); **35**, 4060 (1987).
[21] L. F. Errea, J. M. Gómez-Llorente, L. Méndez, and A. Riera, J. Phys. B **20**, 6089 (1987).
[22] W. Fritsch, Phys. Rev. A **38**, 2664 (1988).
[23] T. G. Winter, Phys. Rev. A **37**, 4656 (1988).
[24] H. J. Lüdde and R. M. Dreizler, J. Phys. B **22**, 3243 (1989).
[25] L. F. Errea, J. M. Maidagan, L. Méndez, and A. Riera, J. Phys. B **24**, L387 (1991).
[26] W. L. Fite, A. C. H. Smith, and R. F. Stebbings, Proc. R. Soc. London Ser. A **268**, 527 (1962).
[27] M. B. Shah and H. B. Gilbody, J. Phys. B **7**, 630 (1974); **11**, 121 (1978).
[28] J. E. Bayfield and G. A. Khayrallah, Phys. Rev. A **12**, 869 (1975).
[29] R. E. Olson, A. Salop, R. A. Phaneuf, and F. W. Meyer, Phys. Rev. A **16**, 1867 (1977).
[30] W. L. Nutt, R. W. McCullough, K. Brady, M. B. Shah, and H. B. Gilbody, J. Phys. B **11**, 1457 (1978).
[31] D. Ćirić, D. Dijkkamp, E. Vlieg, and F. J. de Heer, J. Phys. B **18**, 4745 (1985).
[32] R. Hoekstra, F. J. de Heer, and R. Morgenstern, J. Phys. B **24**, 4025 (1991).
[33] G. J. Frieling, R. Hoekstra, E. Smulders, W. J. Dickson, A. N. Zinoviev, S. J. Kuppens, and F. J. de Heer, J. Phys. B **25**, 1245 (1992).
[34] J. B. A. Mitchell, K. F. Dunn, G. C. Angel, R. Browning, and H. B. Gilbody, J. Phys. B **10**, 1897 (1977).
[35] B. Peart, K. Grey, and K. T. Dolder, J. Phys. B **10**, 2675 (1977).
[36] G. C. Angel, K. F. Dunn, E. C. Sewell, and H. B. Gilbody, J. Phys. B **11**, L49 (1978).
[37] G. C. Angel, E. C. Sewell, K. F. Dunn, and H. B. Gilbody, J. Phys. B **11**, L297 (1978).
[38] B. Peart, K. Rinn, and K. Dolder, J. Phys. B **16**, 1461 (1983).
[39] K. Rinn, F. Melchert, and E. Salzborn, J. Phys. B **18**, 3783 (1985).
[40] M. F. Watts, K. F. Dunn, and H. B. Gilbody, J. Phys. B **19**, L355 (1986).
[41] M. B. Shah and H. B. Gilbody, J. Phys. B **14**, 2361 (1981).
[42] K. Rinn, F. Melchert, K. Rink, and E. Salzborn, J. Phys. B **19**, 3717 (1986).
[43] M. B. Shah, D. S. Elliott, P. McCallion, and H. B. Gilbody, J. Phys. B **21**, 2455 (1988).
[44] D. R. Bates, Proc. R. Soc. London Ser. A **247**, 294 (1958).
[45] C. D. Lin, J. Phys. B **11**, L185 (1978).
[46] B. H. Brandsen, Rep. Prog. Phys. **35**, 949 (1982).
[47] W. Fritsch and C. D. Lin, Phys. Rep. **202**, 1 (1991).
[48] D. R. Bates and R. McCarroll, Proc. R. Soc. London Ser. A **245**, 175 (1958).
[49] A. Riera and A. Salin, J. Phys. B **9**, 2877 (1976).
[50] J. S. Briggs, Rep. Prog. Phys. **39**, 217 (1976).
[51] J. B. Delos, Rev. Mod. Phys. **53**, 287 (1981).
[52] R. McCarroll, in *Atomic and Molecular Collision Theory,* edited by F. A. Gianturco (Plenum, New York, 1982), p. 165.
[53] A. Riera, Phys. Rev. A **30**, 2304 (1984).
[54] G. Hose, preceding paper, Phys. Rev. A **51**, 2199 (1995).
[55] B. C. Garett and D. G. Truhlar, in *Theoretical Chemistry: Advances and Perspectives,* edited by D. Hendersen (Academic, New York, 1981), Vol. 6A, p. 215.
[56] G. Hose, J. Phys. (Paris) Colloq. **50**, C1-111 (1989).
[57] J. D. Power, Philos. Trans. R. Soc. London Ser. A **274**, 663 (1973).
[58] H. Rosenthal, Phys. Rev. Lett. **27**, 635 (1971).
[59] D. R. Bates and T. R. Carson, Proc. R. Soc. London Ser. A **234**, 207 (1956).
[60] G. Hunter and H. O. Pritchard, J. Chem. Phys. **46**, 2146 (1967).
[61] T. G. Winter, M. D. Duncan, and N. F. Lane, J. Phys. B **10**, 285 (1977).
[62] G. Hose (unpublished).
[63] H. Jouin and C. Harel, J. Phys. B **24**, 3219 (1991).
[64] D. Ćirić, R. Hoekstra, F. J. de Heer, and R. Morgenstern, in *Electronic and Atomic Collisions,* edited by H. B. Gilbody, W. R. Newell, F. H. Read, and A. C. H. Smith (Elsevier, Amsterdam, 1988), p. 655.
[65] A. Donnelley, J. Geddes, and H. B. Gilbody, J. Phys. B **24**, 165 (1991).
[66] M. P. Hughes, J. Geddes, and H. B. Gilbody, J. Phys. B **27**, 1143 (1994).
[67] S. Haroche, in *High Resolution Laser Spectroscopy,* edited by K. Shimoda (Springer, Berlin, 1976), p. 253.
[68] G. J. Diebold, Phys. Rev. Lett. **51**, 1344 (1983); Phys. Rev. A **32**, 1485 (1985).
[69] G. S. Agarwal, *Quantum Statistical Theories of Spontaneous Emission* (Springer, Berlin, 1974).
[70] G. Kuritzki and A. Ben-Reuven, Phys. Rev. A **32**, 2560 (1985); **36**, 90 (1987).
[71] H. A. Bethe and E. E. Salpeter, *Quantum Mechanics of One- and Two-Electron Atoms* (Springer, Berlin, 1957), p. 248.
[72] G. Hose (unpublished).
[73] W. Fritsch, R. Shingal, and C. D. Lin, Phys. Rev. A **44**, 5686 (1991).
[74] H. S. Taylor, Adv. Chem. Phys. **18**, 91 (1970).